THE UNIVERSITY OF VIRGINIA

Kinematic dependence of the dilution factor in the SpinQuest experiment E1039 at Fermilab

by

Arthur Conover

A thesis submitted in partial fulfillment for the
degree of Master of Science

to the
Faculty of the
Department of Physics

April 2020

Declaration of Authorship

I, Arthur Conover, declare that this thesis titled, 'Kinematic dependence of the dilution factor in the SpinQuest experiment E1039 at Fermilab' and the work presented in it are my own. I confirm that:

- This work was done wholly or mainly while in candidature for a research degree at this University.
- Where any part of this thesis has previously been submitted for a degree or any other qualification at this University or any other institution, this has been clearly stated.
- Where I have consulted the published work of others, this is always clearly attributed.
- Where I have quoted from the work of others, the source is always given. With the exception of such quotations, this thesis is entirely my own work.
- I have acknowledged all main sources of help.
- Where the thesis is based on work done by myself jointly with others, I have made clear exactly what was done by others and what I have contributed myself.

Signed: 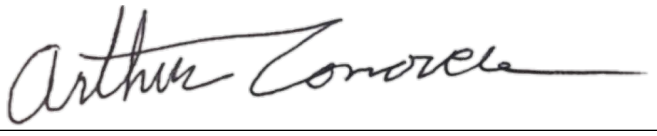

Date: April 29, 2020

Abstract

Thirty years after the "Spin Crisis" began, there is still uncertainty surrounding the spin structure of the nucleon. SpinQuest Experiment E1039 at FermiLab will attempt to probe the internal transverse dynamics of the nucleon via Drell-Yan scattering of a 120 GeV proton beam from a polarized proton target to determine if the orbital angular momentum of the sea-quarks contributes to the overall spin of the nucleon.

In order to understand a leading contribution to the overall systematic uncertainty in this experiment, a study was performed to calculate and evaluate the uncertainty in the dilution factor of the experimental target. This thesis catalogs that effort, highlights where it overlaps with other sources of systematic error, and suggests future work aimed at reducing the overall systematic error of the experiment.

Acknowledgements

I want to thank my advisors Donal Day and Dustin Keller for their guidance and help in creating this thesis. I also want to thank the other members of the Polarized Target Group, especially Daniel Abrams, Zulkaida Akbar, and Joshua Hoskins, and to the entire SpinQuest Collaboration. Thanks also to my parents and to Nicole Story for their help, love, and support.

Contents

List of Figures

Chapter 1

Introduction

Humans have been pondering the nature of matter for millennia. Although Democritus came surprisingly close to the truth 2500 years ago with his atomic theory, until relatively recently the prevailing belief was in the continuity of matter. Before the scientific revolution, most western thinkers still adhered to the Aristotelian model of five elements (water, wind, fire, air, and aether), which combined in different ratios and ways to make everything in the universe.

In the last century, we have greatly advanced our understanding of the composition of matter. J.J. Thomson's discovery of the electron in 1897 began a cascade of discoveries, leading to the model we have today. In the current model, known as the Standard Model, there are seventeen types of particles which interact through three forces. Five of the particles are bosons which mediate the electroweak and strong forces between the other particles (gravity has no known mediator, although the existence of a graviton boson has been posited). The other twelve are fermions, split into three generations: ordinary, exotic and very exotic.

The ordinary generation fermions include the up quark (u), down quark (d), electron (e), and electron neutrino (γ_e). These each also have anti-particles associated with them, which have equal mass and opposite electric charge. Those particles are denoted by a bar over their symbol (i.e. $\bar{u}$). The up quarks and down quarks combine to form long-living hadrons, which make up most of the matter in the universe. Studying the way they combine is now one of the main goals of physics research into matter.

Much of this research is into the way that the interactions of the quarks give rise to the properties of the protons and neutrons they are contained within. These properties include the mass, the magnetic moment, charge density, and the spin of the nucleon, as well as the interactions between nucleons when they collide with other particles.

The best way to probe these particles is through particle scattering. By accelerating particles and colliding them, we can analyze observables such as the cross-section of the particles, which is a measure of the likelihood of a certain process occurring during a collision. By measuring these observable quantities, we can infer the structure and dynamical properties that affect that process.

It has become clear over the past fifty years that the interactions of the particles within the nucleon contribute just as much, if not more, to the nucleon properties as the properties of the individual constituent particles. The mass of the proton, for instance is approximately one-hundred times greater than that of the three quarks that it contains.

Another mystery is the composition of the spin of the nucleon. Known as the spin crisis, for thirty years physicists have known that a large amount of the spin of the proton is unaccounted for based on our current knowledge of the dynamics of the interior of the proton. Using Drell-Yan scattering, SpinQuest will measure the correlation between the angular distribution of the resulting dimuons and the polarized spin of the proton. It will measure the so-called Sivers function asymmetry of $\bar{u}$ and $\bar{d}$ antiquarks within the nucleon. If this asymmetry is non-zero, then the antiquarks must have a non-zero orbital angular momentum (OAM). A non-zero OAM of these charged particles would contribute to the overall spin of the nucleon.

Other experiments, such as those by HERMES[6], COMPASS[7] and JLab [8] have suggested such an asymmetry exists for the valence quarks of the nucleon, but there has not been a high-precision measurement of the asymmetry for sea quarks. The asymmetry is thought to be very small, requiring a very precise measurement. Hence, reducing sources of uncertainty is critical.

By using the Drell-Yan process rather than Semi-Inclusive Deep Inelastic Scattering, it is possible to isolate the sea quarks of the target nucleus. Drell-Yan also has the added benefit that the resulting particles do not fragment, which simplifies signal processing and makes it the cleanest way to probe the Sivers function.

For the experiment, a polarized target of either NH_3 or ND_3 ammonia will be bombarded by 120 GeV protons from the main injector particle accelerator at Fermilab. By using a polarized target, we are able to directly probe the spin degrees of freedom of the target nucleons. In the analysis of these experiments, it is important not only to know the degree of polarization, but also what portion of the target consists of polarizable nucleons.

The portion of the target that can be polarized is known as the dilution factor. The dilution factor appears as a critical part of the analysis, and knowing it with good precision reduces the experiment's ultimate error. The calculation of the dilution factor is, however, non-trivial, as the specific dynamics of the experiment affect its value. This thesis will aim to calculate the dilution factor for the target used in E1039, to reduce the uncertainty in that value, and to create a process that will allow for its simple and accurate calculation in future experiments.

Chapter 2

Background and Motivation

2.1 Nucleon Structure

Since their discoveries, our understanding of the nature of protons and neutrons has not stopped evolving. Once thought to be fundamental particles, we now know that they are composite particles. There is still uncertainty surrounding their internal dynamics, which has attracted a great deal of research.

2.1.1 Parton Theory

In the 1960s, Murray Gell-Man and George Zweig independendly postulated the existence of so-called quarks, which combined in various ways to form hadrons[9][10]. About five years later, Richard Feynman proposed a model of partons to describe hadron collisions, which later proved to overlap with Gell-Man and Zweig's theories[11].

The parton model describes the interior dynamics of hadrons using point-like quarks and gluons as constituent particles. Quarks and antiquarks can combine either into triplets, called baryons, or pairs, called mesons. Each quark has a "color" charge, which can be red, blue, or green. Antiquarks also carry a color charge, which is denoted by anti-red, anti-blue, or anti-green. Any composite particle must be "colorless". This means that when forming a baryon there must be one quark of each color, and when forming a meson there must be a quark and anti-quark of the same color.

According to the parton model, there are two flavors of quarks that make up the vast majority of matter: up quarks and down quarks. An up quark has a charge of $+2/3$ and a down quark has a charge of $-1/3$, and both are spin 1/2. The proton is made of two up quarks and one down quark, and the neutron is made of two down quarks and one up quark. The spin of two quarks is aligned with the spin of the nucleon, and one is anti-aligned. For instance, the wave function of a spin-up neutron is given by:

$$\left|n^{\uparrow}\right\rangle = \frac{1}{6}(2\left|d^{\uparrow}d^{\downarrow}u^{\uparrow}\right\rangle - \left|d^{\uparrow}d^{\uparrow}u^{\downarrow}\right\rangle - \left|d^{\downarrow}d^{\uparrow}u^{\uparrow}\right\rangle) \tag{2.1}$$

This theory has been refined in the past fifty years, and the current theory includes the mediation of the forces between the quarks by gluons, and the existence of virtual quark-antiquark pairs. These pairs pop in and out of existence due to the high energy density in the interior of the nucleon. The pairs are referred to as sea quarks, to distinguish them from the three valence quarks. The gluons are bosons that mediate the strong interaction similarly to the photon mediating the electroweak force. The gluon also carries color charge and has an intrinsic spin of 1, which makes quantum chromodynamics (QCD) more complex to analyze than quantum electrodynamics (QED)[12].

2.1.2 The Spin Crisis

In the original parton model, the spin of the nuceleon was carried entirely by the valence quarks. The stability of nucleon's measured spin seemed to confirm this, as chaotic internal dynamics would seem to add a degree of randomness in the observable. Problems began to arise in the late 1980s, when the European Muon Collaboration measured the valence quark contribution to the spin of the proton. They found that the intrinsic spin of the valence quarks contributed a very small amount to the entire spin. Their analysis found that the spin of the quarks contributed $(14 \pm 9 \pm 21)\%$ of the spin of the proton, which is consistent with zero[13].

More recent studies have found that although the spin of the valence quarks does contribute to the overall spin of the nucleon, the intrinsic spin of the constituent quarks and gluons are not sufficient to account for the entire spin. For that reason, it is now believed that the orbital angular momentum of the partons also

contributes to the spin of the nucleon. Recent studies using lattice quantum chromodynamics (LQCD), a non-perurbative method to solve QCD, estimate that 60% of the spin comes from the intrinsic spins of quarks and gluons, and the remaining 40% comes from the orbital angular momentum of the quarks, as shown in Figure 2.1.

LQCD evaluates QCD by dividing space-time into discrete points, with connecting links between neighboring points. The fermion fields are defined at each point of the lattice, and the gauge fields are defined on the links between the points. This allows QCD to be solved without any assumptions, letting theorists calculate observables from first principles. As the spacing between the points approches zero, the limit of continuous QCD is recovered.

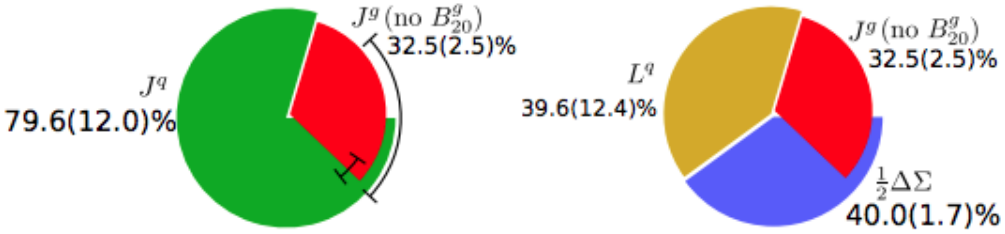

FIGURE 2.1: Spin breakdown of a proton (Wieste et al.)[1]. Approximately 80% of the spin is contributed by the quarks, of which half is from orbital angular momentum of the quarks.

According to a recent calculation by Wieste et al.[1], the majority of the contribution from orbital angular momentum comes from the antiquarks in the nucleon sea, with the valence quarks accounting for a fairly small portion of the spin. In order to test this theory, it is therefore desirable to make a measurement confirming the orbital angular momentum of the sea quarks and that it is indeed non-zero.

2.2 Scattering

When two particles pass close to each other, there is a chance that they will interact and either create new particles or simply alter their paths. By studying these interactions, it is possible to study the particles that participate in those scattering process.

2.2.1 Scattering Cross-Sections

The probability of a specific process occurring when two particles interact is called its cross-section. If it is the probability of the interaction happening with some specified result, it is referred to as the differential cross-section, and if it is integrated over all possible results it is referred to as the total cross-section. Cross-sections are derived from the forces between the two particles. For most processes of interest, this is either the electroweak force using quantum electrodynamics (QED) or the strong force using quantum chromodynamics (QCD).

Composite particles such as nucleons, can act either as a single particle or a collection of particles depending on the context and nature of the interaction. For instance, when a low energy electron scatters off of a proton, it "sees" the proton as a point-like particle. However, if the electron is of sufficiently high energy, it is able to resolve the individual quarks within the proton and probe their distribution.

Precise predictions of the distribution of quarks within composite particles are not obtainable from QCD with current computational methods[14]. For this reason, cross-sections involving nucleons have some uncertainty attached to them due to the uncertainty in quark distributions. By performing experiments involving nucleons and analyzing their results, it is possible to reconstruct these quark distributions, and make better predictions of other cross-sections[15].

2.2.2 Drell-Yan Scattering

When two hadrons collide, it is possible for a quark from one and an antiquark from the other to annihilate, creating a virtual photon which then decays into a dilepton pair. This is known as the Drell-Yan process. Figure 2.2 shows the first-order Feynman diagram for this process[16].

Using the formalism in reference [17], we define the following quantities:

$$q = (q_0, \boldsymbol{q}_T, q_L) \qquad Q^2 = M^2 = (-q)^2 \qquad y = \frac{1}{2} ln \frac{q_0 + q_L}{q_0 - q_L} \tag{2.2}$$

$$x_F = \frac{2q_L}{\sqrt{s}} = x_1 - x_2 \qquad s = (E_1 + E_2)^2 \qquad s x_1 x_2 = M \tag{2.3}$$

Here q is the four-momentum, q_0 is the rest mass, and $\boldsymbol{q}_T$ and q_L are the transverse and longitudinal momenta of the virtual photon in the Drell-Yan process. The

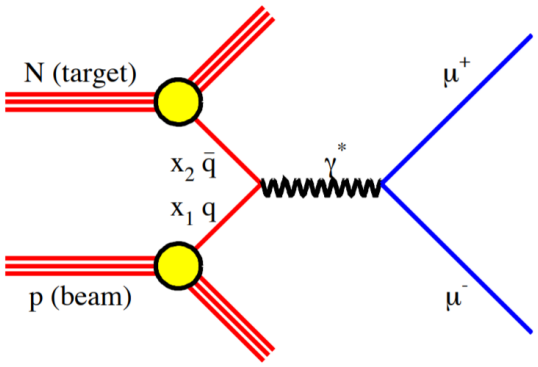

FIGURE 2.2: The first-order Feynman diagram for the Drell-Yan process.

square of the invariant mass of the resultant leptons is equal to Q^2, and s is the square of the center-of-mass energy of the collision. x_F is referred to as the Fermi-x, and x_1 and x_2 are the Bjorken-x for the beam and target, respectively. These can be calculated from the x_F, s and M via

$$x_{1,2} = \frac{1}{2}(\sqrt{x_F^2 + \frac{4M^2}{s}} \mp x_F). \tag{2.4}$$

To first order, the cross-section is dependent only on the quark and antiquark distributions (q and $\bar{q}$) inside the proton as a function of x_1, x_2 and the Q^2 of the collision. The x differential cross-section is given by

$$\frac{d\sigma}{dx_1 dx_2} = \frac{4\pi\alpha^2}{9sx_1x_2}\sum_i e_i^2(q_i^B(x_1,Q^2)\bar{q}_i^T(x_2,Q^2) + \bar{q}_i^B(x_1,Q^2)q_i^T(x_2,Q^2)), \tag{2.5}$$

where e_i is the charge of the specified quark flavor and α is the fine structure constant. Since the cross-section is inversely proportional to s, the Drell-Yan cross section falls off as the energy of the collision increases.

As seen in Figure 2.3, quarks are distributed heavily at larger x values, while antiquarks are distributed at small x values. This means that if we select events that have large x_1 values and small x_2 values, then the quarks from the beam protons and the antiquarks from the target proton are selected. The x-differential cross-section is given by

$$\frac{d\sigma}{dx_1 dx_2} \approx \frac{4\pi\alpha^2}{9sx_1x_2}\sum_i e_i^2 q_i^B(x_1,Q^2)\bar{q}_i^T(x_2,Q^2). \tag{2.6}$$

Due to the charges of up and down quarks (+2/3 and -1/3), this process is dominated by the up quarks in proton-proton collisions and is mixed in proton-neutron collisions. Therefore it is necessary to do proton-proton collisions to probe the distribution of up quarks, and then using that information, it is possible to extract information about the distribution of down quarks from proton-deuteron scattering[18].

2.3 Parton Distributions

Current theory says that the state of each quark can be defined as a probability density in 3-position and 3-momentum space[19]. These distributions are not observable, so instead we must rely on other characterizations for our understanding of the internal dynamics and composition of the nucleon.

2.3.1 Parton Distribution Functions

PDFs characterize the probability density that a particle with a certain longitudinal momentum fraction, x, is found at a specific resolution scale Q^2[20]. Although it is theoretically possible to calculate the PDFs directly using lattice QCD, current computational power is not sufficient[14]. It is therefore necessary to analyze the differential cross-sections of various scattering processes derived from experiment to extract the PDFs.

One method to probe the parton is through deep inelastic scattering of leptons (DIS). Indeed, the first evidence of a substructure of the nucleon was from a DIS experiment in 1968[21][22]. In DIS experiments, a high-energy lepton (electron, muon or neutrino) is scattered off of a hadron and deposits some energy into the hadron (hence inelastic).

By measuring the dynamics of the scattering, the internal dynamics of the hadron can be reconstructed. There are different collaborations who use experimental results to create PDFs, which are then published in packages. This is done by global analysis of hard-scattering data within the framework of perturbative QCD. For one collaboration, the MMHT Collaboration, this is done using data from the Fermilab Tevatron and the CERN Large Hadron Collider.[2] These distributions

can then be sampled using Monte Carlo simulations to predict behaviors and observables of nucleons. [20]

This distribution is typically reported as $f_i^{p,n}(x, Q^2)$, where $Q^2 = (-q)^2$ and x is the Bjorken-x, which represents the fraction of the hadron momentum that the parton contributes, i indicates the flavor of the quark, and p or n indicates the nucleon in question. At lower Q^2, the valence quarks dominate in the parton, and as Q^2 increases the number of quark-antiquark pairs increases, which increases the amount of momentum carried by the antiquarks. An example from the MMHT Collaboration [2] is shown in 2.3.

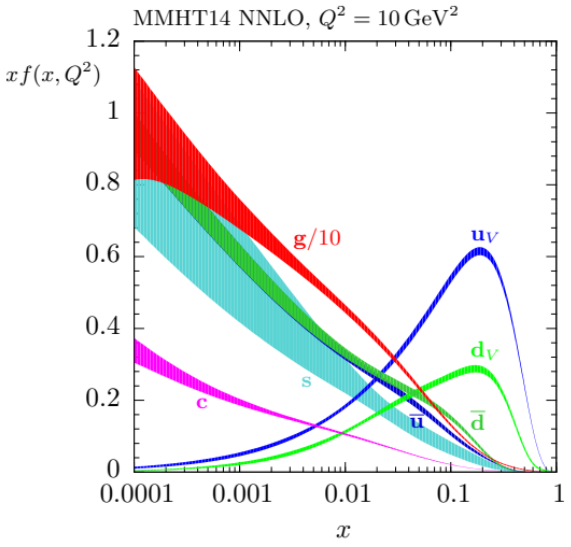

FIGURE 2.3: The leading order MMHT 2014 PDFs for all flavors of quarks at $Q^2 = 10$GeV. Curves are derived by fitting QCD to global hard-scattering data. Uncertainties shown are one standard deviation[2].

2.3.2 Flavor Asymmetry of the Nucleon Sea

Theory does not explicitly predict an equal number of $\bar{u}$ and $\bar{d}$ antiquarks in the nucleon sea, there was no known reason for an asymmetry. Since the quark-antiquark pairs in the sea are created by the energy of the field, and the energy is much higher than the mass of either $\bar{u}$ or $\bar{d}$, it should be expected that they are created at equal rates.

Experiments have shown that there is in fact an asymmetry in the prevalence of the pairs[23]. The NuSea collaboration at Fermilab probed this asymmetry

by measuring the ratio of the Drell-Yan cross-section of proton-deuteron scattering compared to proton-proton scattering. One can relate this ratio to the $\bar{d}/\bar{u}$ asymmetry with the expression

$$\frac{\sigma_{pd}}{2\sigma_{pp}}|_{x_1 \gg x_2} \approx \frac{1}{2}\frac{(1+\frac{1}{4}\frac{d_1}{u_1})}{(1+\frac{1}{4}\frac{d_1}{u_1}\frac{\bar{d}_2}{\bar{u}_2})}(1+\frac{\bar{d}_2}{\bar{u}_2}) \tag{2.7}$$

where subscripts of 1 refer to the beam protons and subscripts of 2 refer to target protons or neutrons [24].

The NuSea analysis found a large asymmetry in the $x_2 < 0.35$ range, as shown in figure 2.4. This asymmetry, and more generally the non-unity ratio of the deuteron-proton cross section ratio will be important effects in analysis of E1039.

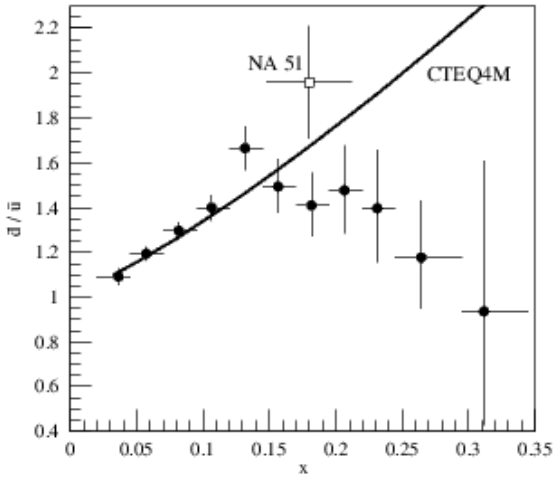

FIGURE 2.4: $\bar{d}/\bar{u}$ asymmetry extracted from deuteron-proton cross section ratio by Fermilab E866. Errors shown are statistical only. A result from NA51 [3] is also shown, as is a prediction of the asymmetry from the CTEQ4M parton distribution function.

2.3.3 Nuclear Modifications of Nucleons

Measurements using DIS show that nuclei do not have the same scattering cross sections when they are in nuclei as when they are free. This is known as the EMC effect.[25] This discovery was surprising, due to the difference in energy scales between DIS energy transfers (GeV scale) and the binding energies of nucleons (MeV scale).

There are many theories that explain this effect, which can broadly be separated into two categories, either using traditional nuclear effects, or using more exotic effects. Tradition effects include binding effects, parton momentum distributions, and pion exchanges. More exotic effects include rescaling of the parton distributions, bag models, or internal structure modification[26][27]. Although not identical, this effect has also been observed in Drell-Yan scattering[28].

Research is ongoing as to the correct explanation of the EMC effect, but while the cause is unknown, the effect is well characterized. It is therefore possible to calculate an effective correction to the PDF of a proton within a nucleus. These corrections depend on both the Bjorken-x and Q^2 of the collisions[29].

In order to make these corrections, a nuclear correction factor is applied to free nucleon PDFs. These corrections can be either be measured using data from both nucleon experiments and nuclear experiments, or be calculated using nucleon PDFs. As an example, the following, from Reference [30] shows the process to calculate the nuclear corrections. At $Q = 1.3GeV$, the nuclear PDFs are parameterized by

$$x f_k(x, Q^2) = c_o x^{c_1}(1-x)^{c_2} e^{c_3 x}(1+e^{c_4}x)^{c_5} \tag{2.8}$$

$$\bar{d}(x, Q^2)/u(x, Q^2) = c_0 x^{c_1}(1-x)^{c_2} + (1+c_3 x)(1-x)^{c_4}, \tag{2.9}$$

where f_k is a stand-in for the PDF of all the varieties of partons present in the nucleon, and the c_n are each specific to the flavor. A correction is made to the c_n for a specific atomic weight A

$$c_n \to c_n(A) \equiv c_{n,0} + c_{n,1}(1 - A^{c_{n,2}}). \tag{2.10}$$

Applying these corrections gives a corrected PDF given by $f_i^{p/A}(x, Q^2)$. The neutron PDF, $f_i^{n/A}(x, Q^2)$m can be related to that of the proton via isospin symmetry. These are then used to make the per-nucleon PDFs for the nucleus, where Z is the atomic number.

$$f_i^{(A,Z)}(x, Q^2) = \frac{Z}{A} f_i^{p/A}(x, Q^2) + \frac{(A-Z)}{A} f_i^{n/A}(x, Q^2). \tag{2.11}$$

By applying these corrections, it is possible to make more accurate predictions of cross-sections and therefore yields of hadron scattering experiments[31].

2.3.4 TMDs and the Sivers Function

The Transverse Momentum Distributions (TMDs) describe the correlation of the transverse momenta of quarks and the transverse spin of the nucleon. Like PDFs, they are measures of the distribution of quarks within the nucleon. Asymmetries in parton distributions are encoded in the TMDs, which allows them to give insight into internal dynamics of the nucleon. Additionally, current computational power is capable of calculating predictions of the TMDs.

The TMDs are derived using the quark-quark correlation function, which can be found in Reference [4]. There are eight leading TMDs, as shown in Figure 2.5.

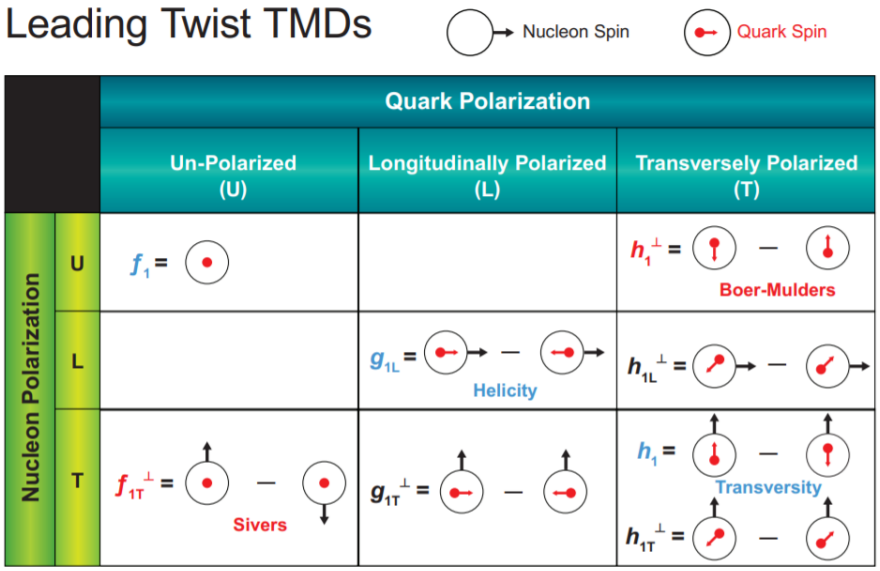

FIGURE 2.5: The quark TMDs, taken from reference[4].

Of particular interest to us is the Sivers function, which represents the relationship between the transverse momentum of an unpolarized parton with the spin of a transversely polarized nucleon. Originally suggested by Dennis Sivers in 1989 to explain asymmetries seen in hadron-hadron collision experiments, a non-zero Sivers asymmetry suggests orbital motion of the partons within the nucleon. This asymmetry is believed to be very small, which has meant that its measurement requires very high-precision and low-error experiments.[32]

2.3.5 Dilution Factor

To extract the Sivers function asymmetry (A_T) from the Drell-Yan scattering in E1039, we use the equation

$$A_T = \frac{2}{f|S_T|} \frac{\int d\phi_S d\phi \frac{dN(x_B, x_T, \phi, \phi_S)}{d\phi_S d\phi} sin(\phi_S)}{N(x_b, x_T)} \tag{2.12}$$

where ϕ_S is the azimuthal angle of the transverse spin orientation of the target, ϕ is the azimuthal angle of the dimuon pair in the Collins-Soper frame (as seen in Figure 2.6), S_T is the transverse component polarization of the target relative to the virtual photon direction, N is the number of events detected in each (x_B, x_T, ϕ, ϕ_T) bin, and f is the dilution factor of the target.

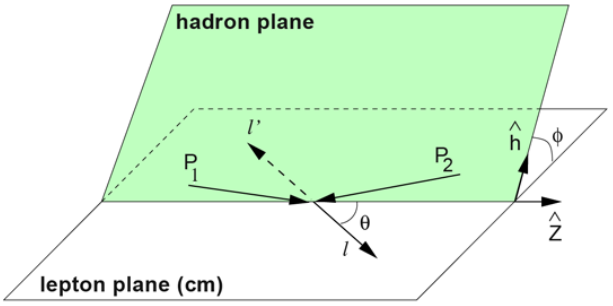

FIGURE 2.6: The Drell-Yan process in the Collins-Soper frame.

The dilution factor is defined as the ratio of polarizable nucleons to total nucleons in a target. For ammonia, this is given by the ratio of the number of hydrogen nucleons to the total number of nucleons. Naively, this is

$$f = \frac{N_H}{N_H + N_N} = \frac{3}{3 + 14} \approx 0.176 \tag{2.13}$$

Where N_H is the number of protons, and N_N is the number of nucleons in nitrogen. However, the picture is more complicated for dynamic systems. A more accurate equation for the dilution factor would be given by

$$f = \frac{3\sigma_H}{3\sigma_H + \sigma_N} \tag{2.14}$$

where σ_H and σ_N are the Drell-Yan cross-sections of hydrogen and nitrogen, respectively.

There are more materials in the experimental beam path than just ammonia, which means the amounts and cross-sections of those materials must also be accounted for when calculating the dynamic dilution factor. Due to this, the dilution factor of the target will actually be given by the equation

$$f = \frac{3\sigma_H}{\sum_A N_A \sigma_A} \tag{2.15}$$

Where A is a stand-in for each nuclei in the beam path. The dilution factor can also be defined for a given kinematic value by substituting the total cross-sections with the differential cross-sections of each nuclei. This would then be given by

$$f = \frac{3d^4\sigma_H(x_B, x_T, \phi, \phi_T)}{\sum_A N_A d^4\sigma_A(x_B, x_T, \phi, \phi_T)}. \tag{2.16}$$

Using numerical integration of the Drell-Yan cross-sections, this will be calculated in Chapter 4 of this thesis.

Chapter 3

Tests of Monte-Carlo Femptobarn

3.1 Monte Carlo Femptobarn

When faced with probabilistic processes or non-analytically solvable integrals, it is often useful to turn to Monte Carlo simulations. In this case, we are in fact faced with both: the cross-sections are dependent on the probabilistic PDFs, and are given by complex-valued, non-analytical integrals.

Monte Carlo simulations sample probability distribution functions in order to create a large sample of events which can then be used to give numerical results. This allows predictions to be made using theories that are too complex for direct analysis. This is the process we will use to calculate differential cross-sections for Drell-Yan scattering.

The program used in these analyses is Monte Carlo for FeMtobarn Processes (MCFM). It is a parton level Monte Carlo program that samples parton distribution functions to calculate cross-sections for hundreds of processes in hadron colliders. These calculations can be done at leading order (no loops in Feynman diagrams), next-to-leading order (one loop corrections), or in some cases next-to-next-to leading order (two loop corrections) in QCD. Higher order calculations are more accurate, but require significantly longer computer time to achieve the same precision as leading-order calculations.

3.1.1 MCFM Cross-Section Calculation

MCFM uses a subtraction method that allows for numerical NLO calculations of QCD while avoiding the singularities that are generally encountered when using one-loop corrections[33]. The NLO cross-section is given by

$$\sigma = \sigma^{LO} + \sigma^{NLO}. \tag{3.1}$$

The LO contribution to the cross-section can be calculated using the Born approximation,

$$\sigma^{LO} \equiv \int_m d\sigma^{LO} = \int_m d\sigma^B, \tag{3.2}$$

where m is the number of partons in the final state, and the integral is evaluated in $4 - \epsilon$ dimensions. This integrand is entirely real, allowing this integral to be calculated numerically. The NLO part of the cross section can be split into two parts,

$$\sigma^{NLO} \equiv \int d\sigma^{NLO} = \int_{m+1} d\sigma^R + \int_m d\sigma^V, \tag{3.3}$$

where $d\sigma^R$ is the real exclusive cross-section with $m+1$ partons in the final state and $d\sigma^V$ is the virtual one-loop correction to the process with m partons in the final state. These both diverge when evaluated in $d = 4$, but their divergences cancel. Computational integration of each is not directly possible, so the integrals need to be redefined in order to calculate them. This can be done by using the subtraction method, which involves the identity

$$d\sigma^{NLO} = [d\sigma^R - d\sigma^A] + d\sigma^A + d\sigma^V, \tag{3.4}$$

where $d\sigma^A$ is an approximation of $d\sigma^R$ that, in d dimensions, has the same pointwise singular behavior as $d\sigma^R$. This allows it to behave as a counterterm, cancelling the singularity. Thus,

$$\sigma^{NLO} = \int_{m+1} [d\sigma^R - d\sigma^A] + \int_{m+1} d\sigma^A + \int_m d\sigma^V. \tag{3.5}$$

The first term is can now be numerically integrated in four dimensions. The second and third terms can then be combined by analytically integrating the last term, which can then be used to cancel the singularity in the second-to-last term. This

means that the calculation can be written

$$\sigma^{NLO} = \int_{m+1} [(d\sigma^R)_{\epsilon=0} - (d\sigma^A)_{\epsilon=0}] + \int_m [d\sigma^A + \int_1 d\sigma^V]_{\epsilon=0}. \tag{3.6}$$

These can then be numerically integrated by sampling partonic events[34].

MCFM does this by sampling a user-specified PDF, using the VEGAS algorithm which allows events to be sampled at a higher rate in areas of interest. To do this, the program runs several iterations of the simulation to condition the algorithm and identify the part of parameter-space that contributes the most to the integral, and then runs through more iterations where more events are sampled in that area. The events are then weighted, giving a higher precision integral with fewer events[33][35].

Users input the energy, QCD scale, and particles involved in the collision (pre-programmed are protons, anti-protons and nuclei, other hadrons may be added by the user). Additionally, the user may specify dynamics cuts, which specify which events are used in final calculations. For instance, for the Drell-Yan process it is required that the resulting particles have an invariant mass greater than zero to prevent the virtual photon from becoming physical.

3.1.2 Data Output

Results from MCFM can be outputted into ROOT, gnuplot or Topdrawer scripts, or simply written to a .dat file. For each process, there are a number of pre-programmed differential cross-section histograms outputted. These include mass, momentum, and angle of scattering differential cross-sections.

Errors for these values are also reported by MCFM, which include simple statistical error and PDF error. The simple statistical error has a $\frac{1}{\sqrt{N}}$ dependence, and the PDF error is propogated from errors reported by the PDF collaborations.

It is also possible to create user-generated histograms using the four-momenta of each event output. For Drell-Yan, it was necessary to create a user-generated output to calculate the x values for each event, as shown below.

$$\tau = \frac{m^2_{\mu^+\mu^-}}{s} \tag{3.7}$$

$$p_{L,max} = \frac{\sqrt{s}(1-\tau)}{2} \tag{3.8}$$

$$x_F = \frac{p_L^{\mu^+} + p_L^{\mu^-}}{p_{L,max}} \tag{3.9}$$

$$x_B = \frac{1}{2}(\sqrt{x_F^2 + 4\tau} + x_F) \tag{3.10}$$

$$x_T = \frac{1}{2}(\sqrt{x_F^2 - 4\tau} + x_F) \tag{3.11}$$

Here, $m_{\mu^+\mu^-}$ is the invariant mass of the dilepton pair, s is the square of the center-of-mass energy of the scattering, $p_{L,max}$ is the maximum possible longitudinal momentum of the dilepton pair, x_f is the Fermi-x, and x_B (x_T) is the beam (target) Bjorken-x.

At this point, it was then possible to calculate the x- and mass-dependent Drell-Yan differential cross-sections, and from them calculate the dynamic dilution factor for E1039. For more complete directions on the use of MCFM, refer to Appendix A of this thesis.

3.2 Systematic Error

In order to determine the accuracy of MCFM and to establish a systematic uncertainty associated with its calculations, it was necessary to perform several tests of the system by comparing simulated data to real data. By doing this, calculations done using the produced cross-sections can account for the error that arises from the simulations.

A number of tests, ranging in energy scale and target material, were performed. By analyzing these and comparing to published data it was possible to estimate the systematic error associated with the cross-section calculations done by MCFM.

Four tests were done: two qualitative and two quantitative. The two qualitative tests were comparisons to cross-section data from experiments at different center-of-mass energies. These were done as a quick check of the viability of MCFM as it pertains to Drell-Yan cross-sections. Since the dilution factor is a ratio of

cross-sections, the value of the cross-sections are not as important as the shape of the curve of the differential cross-sections, or the ratio between cross-sections for different targets.

The two quantitative tests done were comparisons to cross-section ratios. These were chosen to check how MCFM handles the two most pertinent effects for nuclear cross-sections, those being the $\bar{d}/\bar{u}$ asymmetry and the EMC effect. Cross-sections were reproduced using MCFM and then the ratios of those cross-sections were compared to experimentally reported ratios.

The discrepancy between these values was calculated and then averaged over values in each experimental x_T bin. The deviation from unity was taken to be the systematic error arising from the MCFM calculations for that process.

3.2.1 CMS Cross-Section

The first comparison was to a recent mass differential cross-section measurement by the CMS collaboration at CERN[5]. The data was collected using a 13 TeV center-of-mass energy, over a dilepton mass range from 15 GeV to 4000 GeV. In order to narrow the scope, cross-sections were compared in the 15 GeV to 150 GeV range. The most important part of this test was determining if the simulation was able to replicate the Z-boson peak, which corresponds to the production of the Z-boson and its subsequent decay. This peak occurs at the Z-boson mass and can be used to probe the coupling of the Z-boson to quarks.

MCFM generated twenty million events (fifty iterations of four-hundred thousand each) by sampling the CT14 PDFs[36]. Ten iterations were used to condition the VEGAS grid, and forty were used to calculate cross-sections. MCFM averages over those forty iterations to reduce statistical error of the reported differential cross-sections.

Although the CMS comparison provided confidence that MCFM was a viable framework for the calculation of Drell-Yan cross-sections, it is at a vastly different energy scale than E1039. While CMS had a center-of-mass energy of 13 TeV, E1039 will have a center-of-mass energy of only 15 GeV, three orders of magnitude lower.

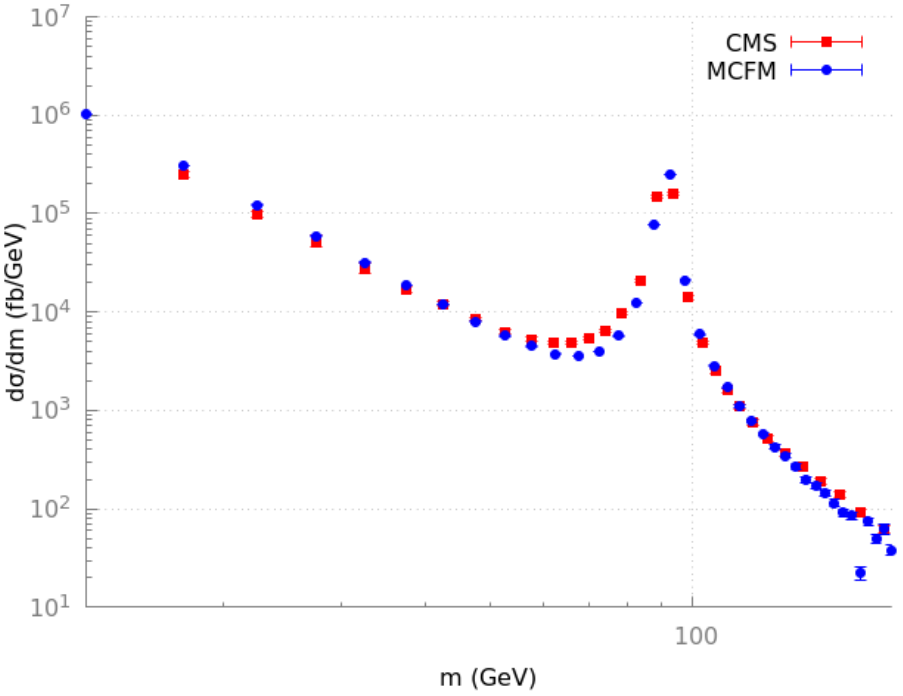

FIGURE 3.1: MCFM comparison to CMS Drell-Yan cross-section. Errors shown are statistical only for CMS data and are outputted errors for MCFM. Data is taken from reference [5].

3.2.2 Low-Energy Cross-Section

In order to test MCFM at lower energy, it was compared to data from an older experiment, E772 at Fermilab. The experiment used a 800 GeV beam, which corresponds to a 38 GeV center-of-mass energy. This is on the same order of magnitude as E1039, and the experiments were done with a similar detector. In fact, many of the parts from that detector have been re-purposed for the E1039 detector[37].

The Drell-Yan range of study for lower energies is typically confined to 4 GeV$<$ $M_{l^-l^+} < 9$ GeV due to J/Ψ production around 3 GeV and the Υ process around 10 GeV. Therefore, this was the range in the data used compare to MCFM. The experiment used a liquid ^{2}H target was used, so the cross sections were calculated with a deuteron target and proton beam. The Monte Carlo simulation was done using the same program settings as the CMS analysis.

There appears to be some non-random behavior in the comparison, namely the ratio is higher in the middle of this mass range than on either the high or low end. When re-binned into 1 GeV width bins, there is good agreement between

experiment and simulation for 3-4 GeV and 7-8 GeV. The 5-6 GeV and 6-7 GeV bins, however, are approximately 7% and 4% higher in MCFM than those from the experiment. See Figures 3.2 and 3.3.

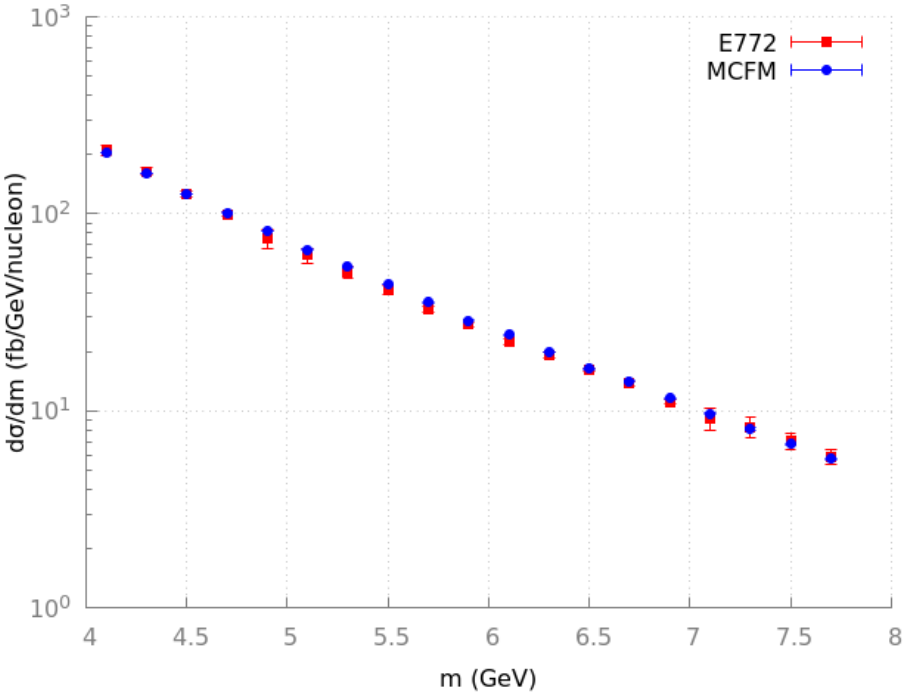

FIGURE 3.2: MCFM and E772 calculated mass differential cross-sections for proton-deuteron Drell-Yan scattering. Errors shown are MCFM error and experimental statistical error.

This effect is likely due to the cuts made in the experiment. The analysis used mass cuts, which allow for events from other processes to leak into the data analyzed. The reported data from E772 did not include a systematic error of 2%, which would extend the . Since the J/Ψ and Υ processes produce events on the outer edges of this range, it is expected that the experimentally reported cross-sections will be higher in those ranges. Considering this, the agreement between the generated and measured cross-sections are encouraging.

Taking that into account, it seems that MCFM reports approximately a 5% higher cross-section in regions where we can directly compare. This may be pertinent for yield predictions, but since the dilution factor is a ratio of differential cross-sections, this error would cancel itself, as it appears in both the numerator and denominator of the ratio.

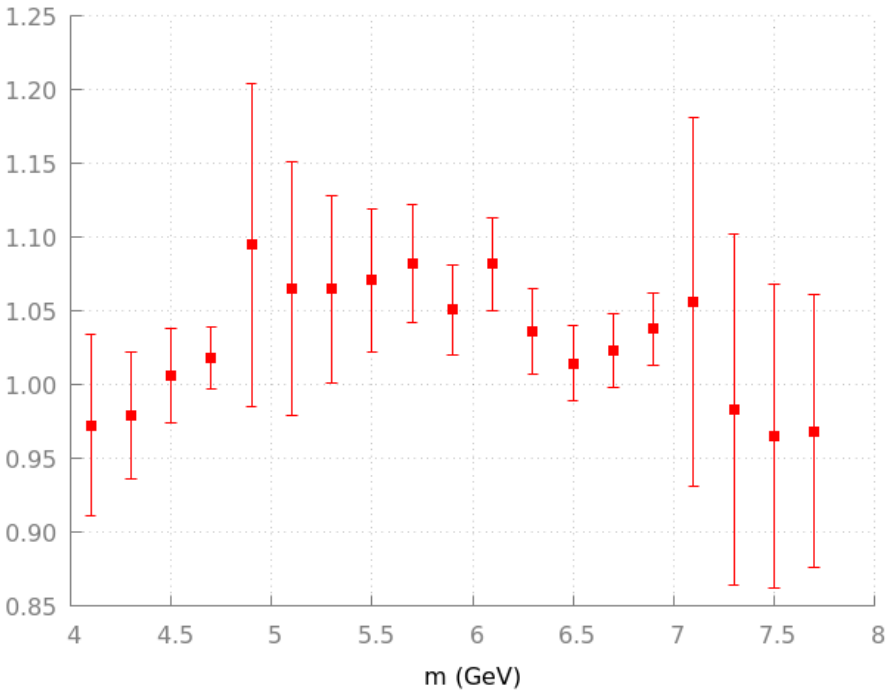

FIGURE 3.3: Ratio of Monte Carlo to experimental cross sections. Values reported are MCFM cross-section divided by the E866 cross-section data. Errors shown are propagated from MCFM error and experimental statistical error. Only five of the twenty bins are more than 1σ from unity.

3.2.3 Proton-Deuteron Cross Section Ratio

Important in this analysis is the difference in cross-sections between protons and neutrons. In order to differentiate between the cross-sections of nuclei and the proton, MCFM needs to be consistent with published data for this effect.

The main source of difference between proton and deuteron differential cross-sections at these kinematics is the $\bar{d}/\bar{u}$ asymmetry in the nucleon sea, as studied by E866 at Fermilab. This again was done using an 800 GeV beam, 38 GeV center-of-mass energy, and a similar detector apparatus.

This comparison involved two MCFM calculations using the same settings as the other analysis, one for the proton differential cross-section and one for the deuteron differential cross-section. See Figure 3.4.

Comparing these results, we find excellent agreement between experimental and calculated ratios, especially for $x_t > 0.1$, which is the kinematic range of interest in E1039. For each experimental data point, a ratio of the experimental value and the MCFM calculated value was found, as shown in Figure 3.5.

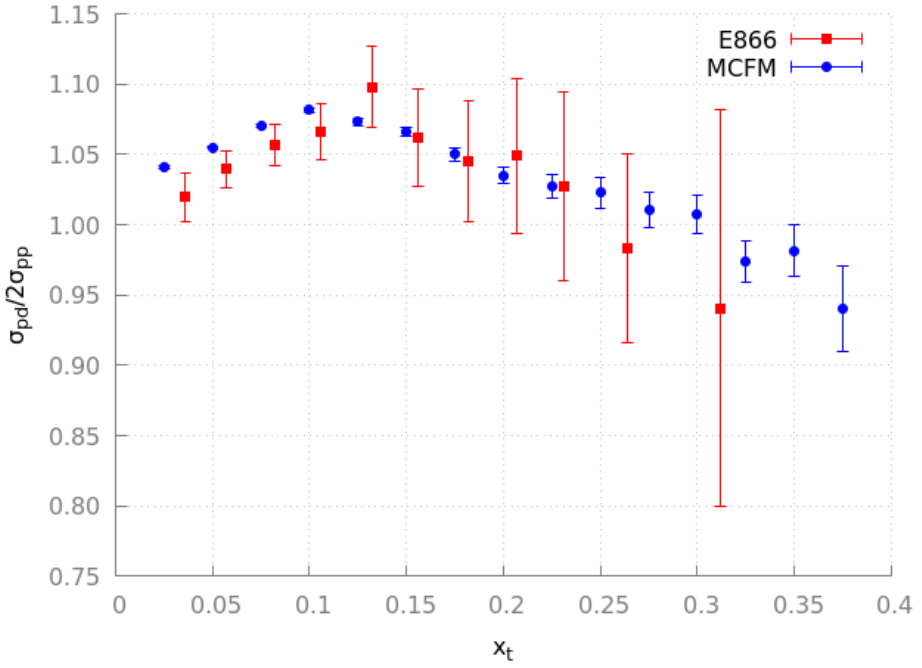

FIGURE 3.4: Ratio of per-nucleon x_t-differential cross-sections of proton-deuteron and proton-proton Drell-Yan scattering. Purple data points are from MCFM simulations, while green data points are from FermiLab experiment E866. Errors shown are purely statistical for E806 and MCFM reported error.

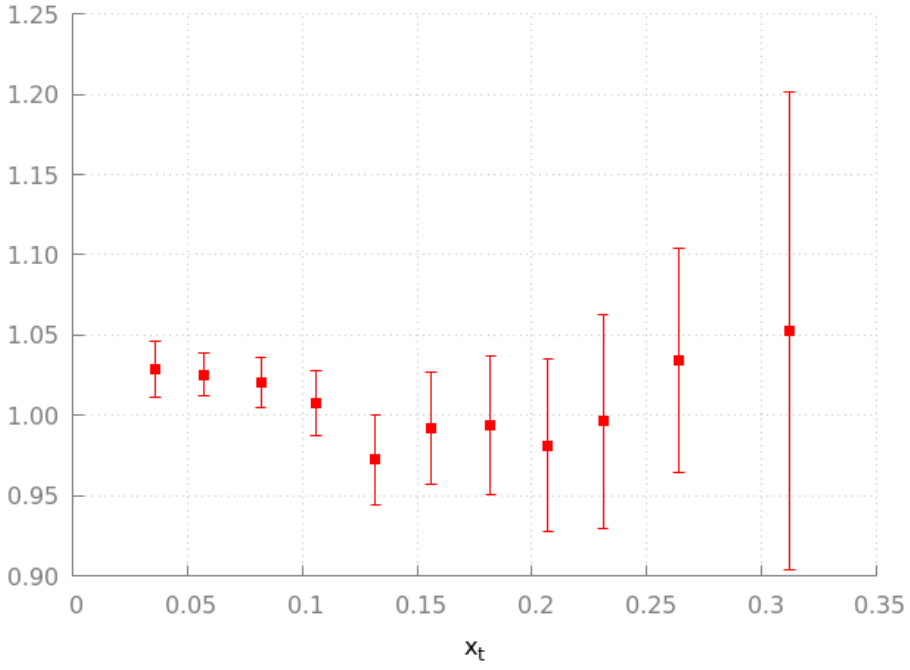

FIGURE 3.5: Ratios of MCFM calculated ratio and experimental ratio of per-nucleon x_t-differential cross-sections of proton-deuteron and proton-proton Drell-Yan scattering. Errors shown are propogated from error of both MCFM and experimental data.

The ratios were grouped into the E1039 bins and each bin had its cross-section and error weighted average calculated, using the equation

$$R_j = \frac{\sum_i R(x_i)\sigma(x_i)/\delta_i}{\sum_i \sigma(x_i)/\delta_i} \tag{3.12}$$

where R is the ratio of MCFM to experimental values, δ_i is the error in the ratio, j refers to the bin number, and i refers to the discrete x_t values. These are then compared to unity, as listed in Table 3.1.

Bin	Deviation (%)
0.10-0.16	0.5
0.16-0.20	1.0
0.20-0.24	1.5
0.24-0.6	2.0

TABLE 3.1: Deviation of MCFM values from experimental values due to proton/deuteron ratio in x_t for E1039

This source of error will only be pertinent for NH_3, since the issue at hand is the difference between free protons and neutrons. The effect contributes a very small amount of systematic uncertainty for small x_t, and increases with x_t.

Since NH_3 has both free protons and nuclei with neutrons, this will be a source of error. For ND_3 this source of error will be zero, since there are no free protons and all target materials are nuclei.

3.2.4 Nuclear Dependence

Of equal importance to the analysis is the effect of high atomic masses on the Drell-Yan cross-section. This effect is mainly due to the EMC effect, which MCFM accounts for by applying a mean-field correction to the parton PDFs. Since recent studies suggest that short-range correlation theories are more accurate[38], it is important to check that the predictions are accurate.

E772 at Fermilab again provides good data to check the Monte Carlo. Using ^{2}H, C, Ca, Fe, and Z targets, the experiment looked at the ratio of heavy nucleus cross-sections to deuteron cross sections. Using MCFM with the same settings as prior tests, these cross-section ratios were reproduced, as shown in Figures 3.6 to 3.9.

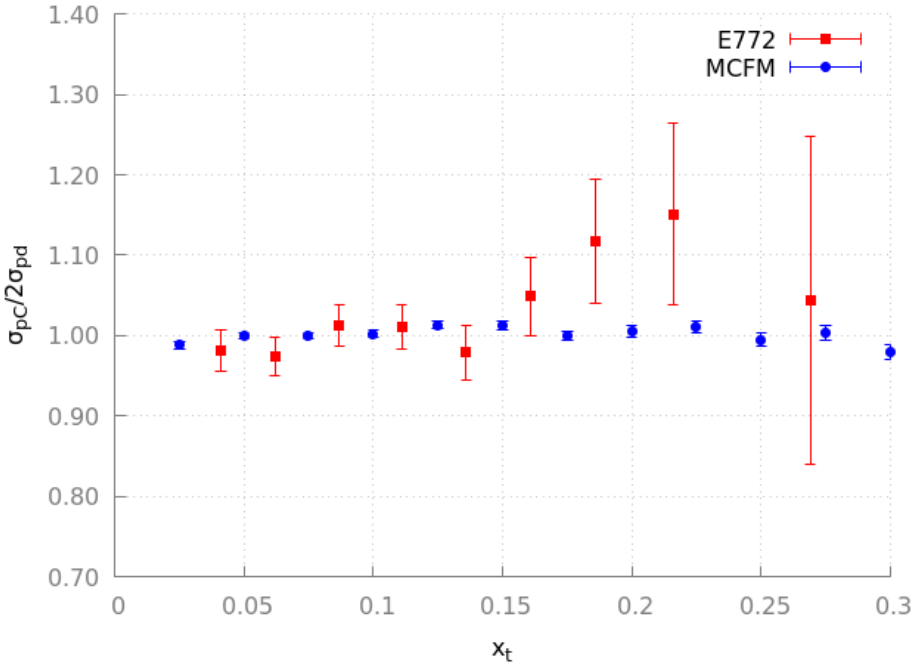

FIGURE 3.6: Ratio of Carbon to deuteron differential cross-section. Errors shown are MCFM reported and statistical for experimental value.

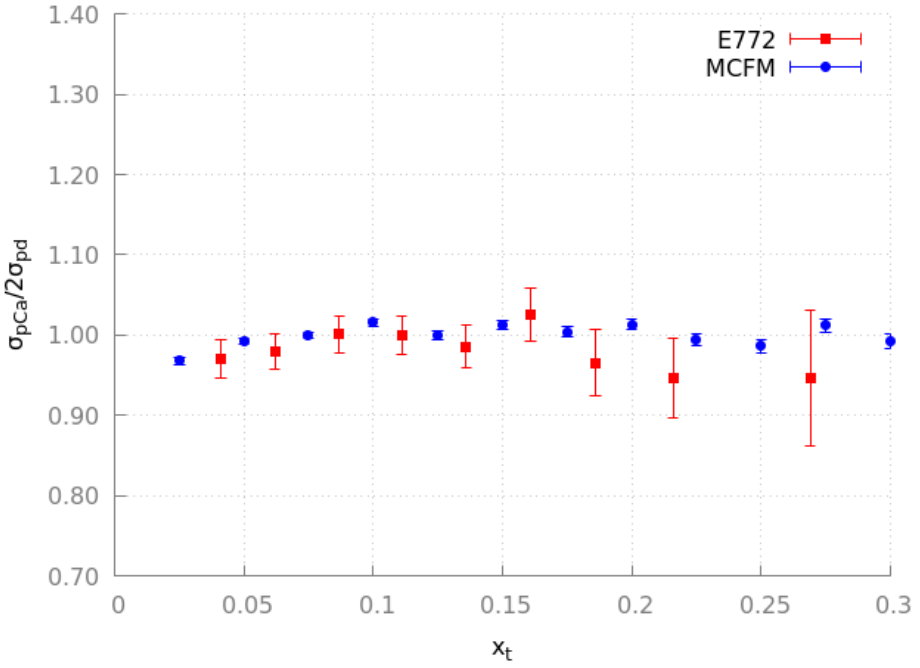

FIGURE 3.7: Ratio of Calcium to deuteron differential cross-section. Errors shown are MCFM reported and statistical for experimental value.

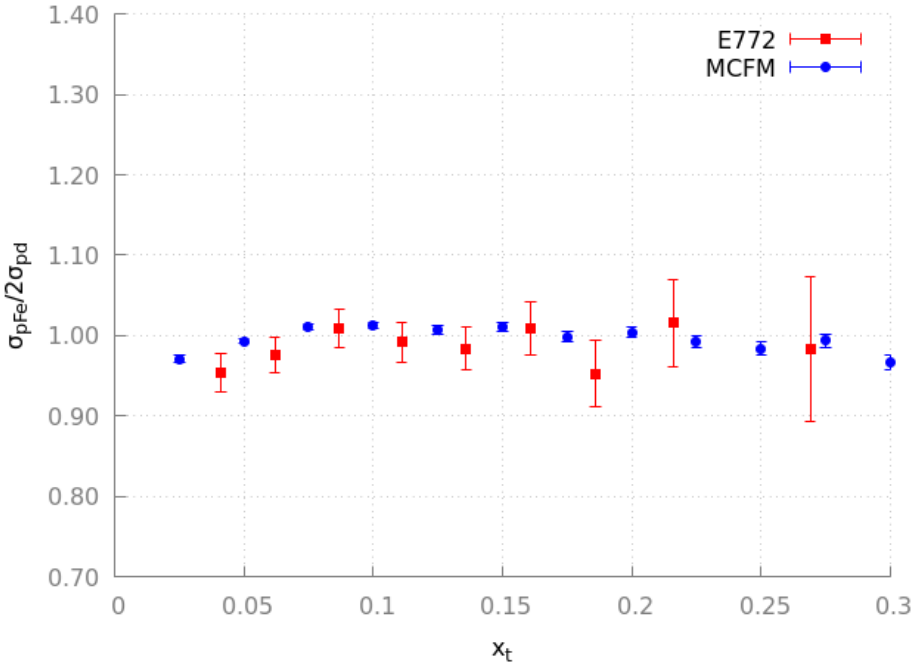

FIGURE 3.8: Ratio of Iron to deuteron differential cross-section. Errors shown are MCFM reported and statistical for experimental value.

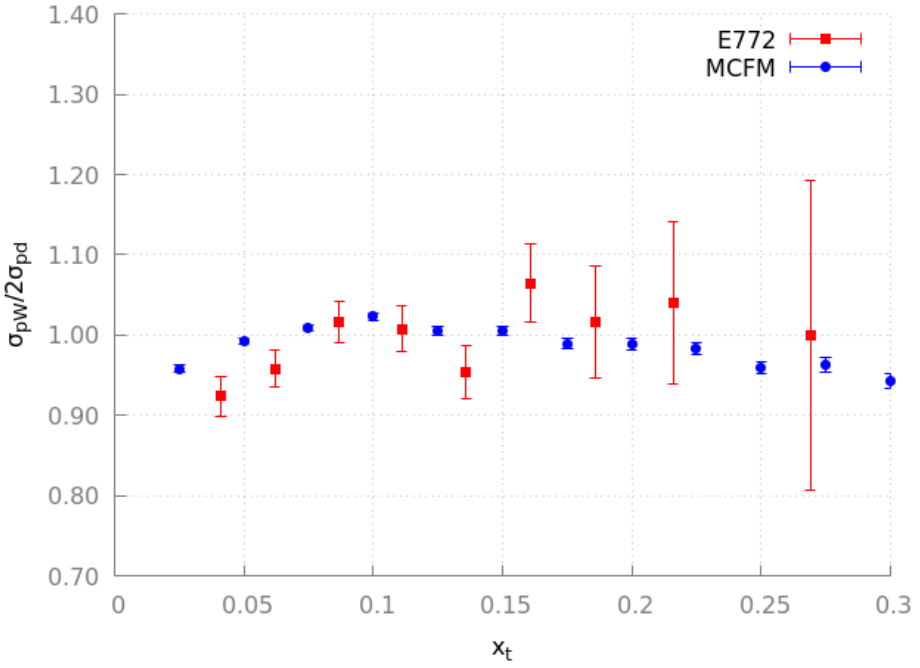

FIGURE 3.9: Ratio of Tungsten to deuteron differential cross-section. Errors shown are MCFM reported and statistical for experimental value.

Like with the E866 comparison, these calculated ratios were compared to the experimentally reported ratios, as shown in Figure 3.10. Those ratios were then used in the same was as before to establish the error and cross-section weighted average for each E1039 bin.

These averages were then compared to unity to establish the deviations shown in Table 3.2. There was agreement between the calculated values and the measured values in all bins, with a higher level of agreement in the lower x-value bins.

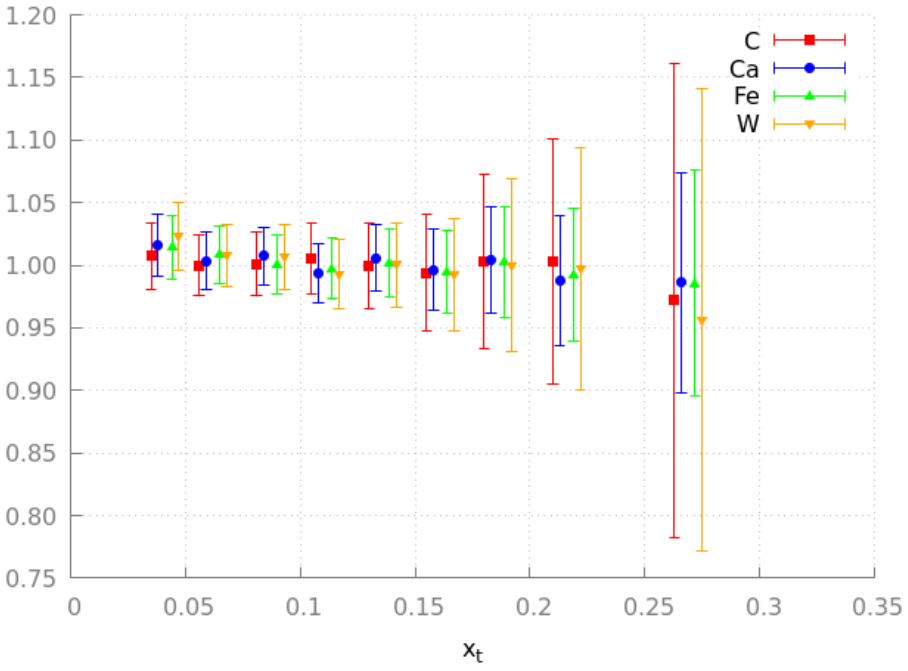

FIGURE 3.10: Ratio of MCFM predicted heavy nucleon ratios to E772 heavy nucleon ratios. Errors shown are propagated from errors from MCFM and experimental data.

Bin	Deviation (%)
0.10-0.16	0.5
0.16-0.20	0.5
0.20-0.24	0.5
0.24-0.6	1.5

TABLE 3.2: Deviation of MCFM values from experimental values due to the EMC effect for the x_t bins for E1039.

As with the uncertainty arising from the $\bar{d}/\bar{u}$ asymmetry, the larger value x bins have a larger degree of uncertainty. It seems likely that this is mostly due to the smaller values of the differential cross-section at higher x values, which increases the statistical uncertainty, both in the experiment and in the Monte-Carlo.

3.3 Statistical Error

As a Monte-Carlo simulation, MCFM is able to achieve arbitrarily high precision for cross-section calculations. It would be expected that the statistical uncertainty would therefore be inversely proportional to the square root of the number of Monte Carlo sampling events.

To confirm this, a quick check was done by calculating the overall cross-section of Drell-Yan proton-proton scattering with different numbers of events, starting at 800 and increasing by factors of two. The reported statistical error was plotted against the number of events, as seen in figure 3.11. Plotted alongside is a fit given by

$$\delta = \frac{A}{\sqrt{n}} \tag{3.13}$$

Where A is an arbitrary constant and n is the number of events per iteration.

Noteworthy from this analysis is that for runs with fewer than about ten thousand events per iteration the error is greater than what would be expected based on the statistical analysis. This may be due to the fact that the VEGAS grid is not as well conditioned, and the program accounts for that in its uncertainty output.

Since cross-sections will be split into four bins, the statistical error for each bin will be approximately twice the magnitude of the total cross-section. Using that data, to achieve precision of 0.1%, approximately 400,000 events per iteration will be required.

3.4 Conclusions

By combining the deviations found due to the $\bar{d}/\bar{u}$ asymmetry and the EMC effect, it is possible to estimate the total systematic uncertainty that will be associated with MCFM predictions of the dilution factor. Since the dilution factor is calculated via a ratio of cross-sections, the error in the absolute cross-section will not contribute to the overall systematic error. These errors are due exclusively to the calculation, assuming perfect accuracy in the measurement of the composition of the target. These total errors are reflected in Table 3.3.

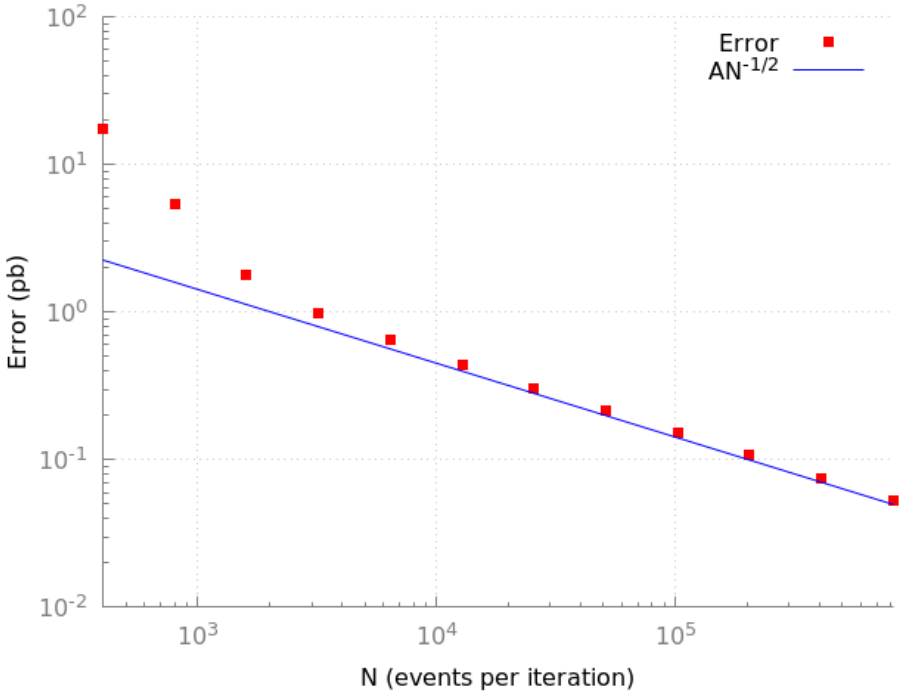

FIGURE 3.11: Reported error of MCFM Drell-Yan proton-proton cross-section calculation vs sampling events.

Bin (x_T)	$\bar{d}/\bar{u}$ (%)	EMC (%)	NH_3 Error (%)	ND_3 Error (%)
0.10-0.16	0.5	0.5	0.7	0.5
0.16-0.20	1.0	0.5	1.1	0.5
0.20-0.24	1.5	0.5	1.6	0.5
0.24-0.6	2.0	1.5	2.5	1.5

TABLE 3.3: Summary of systematic error arising from MCFM by bin. Error for NH_3 is the pythagorean sum of $\bar{d}/\bar{u}$ and EMC deviations, while ND_3 error is entirely from the EMC effect. There may be a degree of double-counting in NH_3 error, since the $\bar{d}/\bar{u}$ asymmetry will also affect the cross-sections of heavy nuclei.

These calculations were made assuming there was not any systematic error in the experiments that would shift the ratios in one direction. This assumption is justified by the similarity of the detector to be used in E1039 to those used in E772 and E806.

Statistical errors from MCFM can be made arbitrarily small. An arbitrary sub-0.1% statistical error in per-bin cross-section can be achieved by running ten conditioning iterations and forty statistical iterations using 400,000 iterations per iteration.

Chapter 4

Results and Future Work

4.1 Dilution Factor Calculations

In order to lower the systematic error associated with SpinQuest E1039, it is desirable to know the dilution factor of the target to high precision and accuracy. To that end, MCFM was used to calculate the dynamics-dependent dilution factors for both ammonia (NH_3) and deuterated ammonia (ND_3).

4.1.1 x_T-Dependent Dilution Factor

By calculating the x_T-differential cross-sections for the elements in the target, it is possible to calculate an x_T-dependent dilution factor. This calculation is fairly simple, for NH_3 the dilution factor is given by

$$f(x_T) = \frac{3\frac{d\sigma_p}{dx_T}}{3\frac{d\sigma_p}{dx_T} + \frac{d\sigma_N}{dx_T}} \tag{4.1}$$

Differential cross-sections were generated using MCFM, using the CT14 parton distribution functions, sampling 400,000 events per iteration and averaging over 40 iterations after using 10 iterations to conditon the VEGAS integration grid. The events were cut if the dimuon mass was below 4 GeV or if x_F was negative. These events were grouped into x-bins with width 0.01 in the range $0.1 \leq x_T \leq 0.6$.

These cross-sections were then put into a spreadsheet which calculates the x_T-dependent cross-sections of ammonia and uses that to calculate the dilution factor. This is done by dividing the cross-section of three hydrogen atoms by the cross-section of the ammonia. Error in the ammonia cross-section was propagated from the error in nitrogen and hydrogen cross-sections, and the statistical error in the dilution factor rose from that error.

These x_T-dependent dilution factors were then re-binned into the E1039 experimental x_T bins. This re-binning was done with a cross-section weighted average, so that in each bin the lower values of x_T, which have higher cross-sections, influenced the dilution factor of the bin more than the higher values of x_T.

The ammonia dilution factors for the E1039 x_T-bins are shown in Figures 4.1 and 4.2. This dilution factor does not account for any other materials in the target. The values are also listed in Table 4.1.

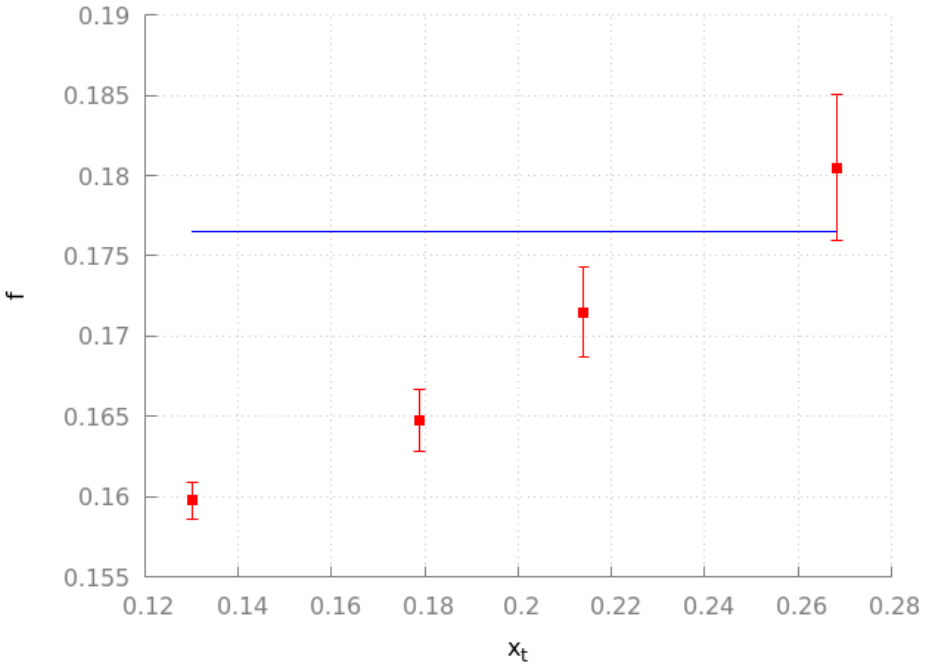

FIGURE 4.1: NH_3 dilution factor for E1039 x_T-bins. Also plotted is the static dilution factor of $\frac{3}{17} \approx 0.176$. Errors shown are both statistical and systematic.

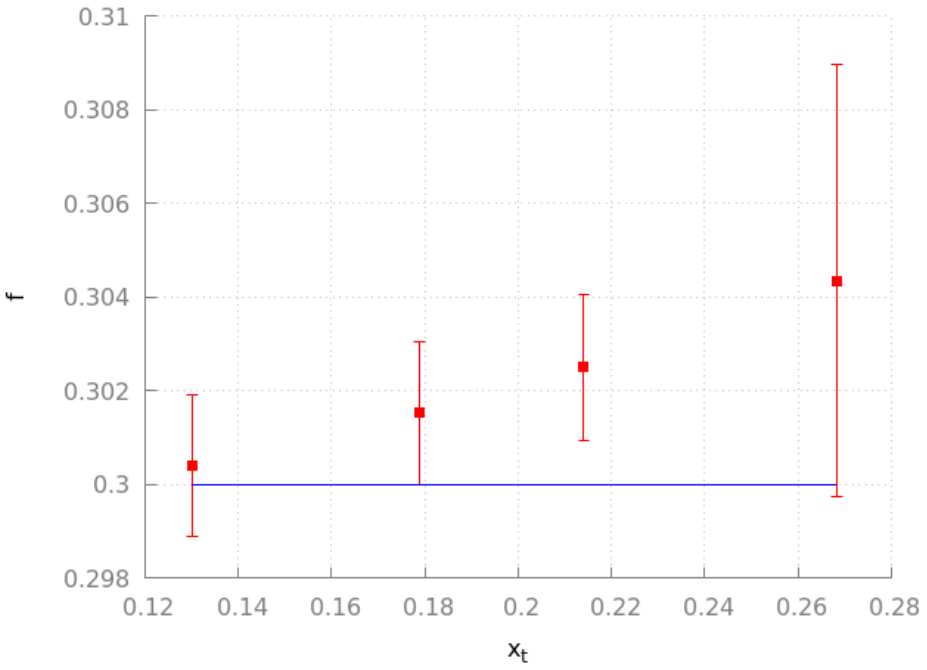

FIGURE 4.2: ND_3 dilution factor for E1039 x_T-bins. Also plotted is the static dilution factor of $\frac{6}{20} = 0.3$. Errors shown are both statistical and systematic.

x_T	NH_3	ND_3
0.10-0.16	0.160 ± 0.001	0.301 ± 0.001
0.16-0.20	0.165 ± 0.002	0.3019 ± 0.0015
0.20-0.24	0.171 ± 0.003	0.3027 ± 0.0015
0.24-0.60	0.180 ± 0.004	0.304 ± 0.005

TABLE 4.1: x_T-dependent dilution factors for pure ammonia in the E1039 experiment. Errors are both statistical and systematic.

When dynamics are taken into consideration, the dilution factor for NH_3 is lower for the bins where $x_T < 0.24$ than the naive static dilution factor of 0.176. For ND_3 the dilution factor is higher across the range than the naive static dilution factor of 0.3. This seems to be due to two effects with opposite effects. The $\bar{d}/\bar{u}$ asymmetry makes the proton differential cross-section relatively lower at low x values, and nuclear per-nucleon cross-sections decrease as the atomic mass increases.

For both NH_3 and ND_3, the dynamic dilution factor is statistically different from the static dilution factor. For NH_3, there is a statistically significant trend increasing over the range, but for ND_3 the errors overlap for all four bins. Although the magnitude of the ND_3 uncertainty is smaller than the uncertainty for NH_3, the value of the dilution changes far less over the range. The difference between the

dilution factors for the largest and smallest bin is approximately ten times greater in NH_3 as compared to ND_3 (11% versus 1.3%).

4.1.2 Mass-Dependent Dilution Factor

As discussed in Chapter 2, Drell-Yan scattering cross-sections are also dependent on Q^2, which in Drell-Yan is equivalent to the square of the mass of the virtual photon that decays into the dilepton pair. Since Q^2 is equivalent to M_{ll}^2, a mass-dependent dilution factor is equivalent to a Q^2-dependent dilution factor.

By calculating the dimuon mass differential cross-sections of the nuclei, it is therefore possible to calculate the mass-dependent dilution factor in the exact same way as was done for the x_T-dependent dilution factor. Ammonia cross-sections were calculated, used to calculate the dilution factor, and had their errors propagated to the error in the dilution factor.

This was done with similar simulations as the x_T-dependent dilution factor, but did not have the 4 GeV mass cut. Figures 4.3 and 4.4 show the mass-dependent dilution factors for NH_3 and ND_3 over the dimuon mass range 3 GeV to 9 GeV, grouped into bins with width 1 GeV. These values are also shown in Table 4.2.

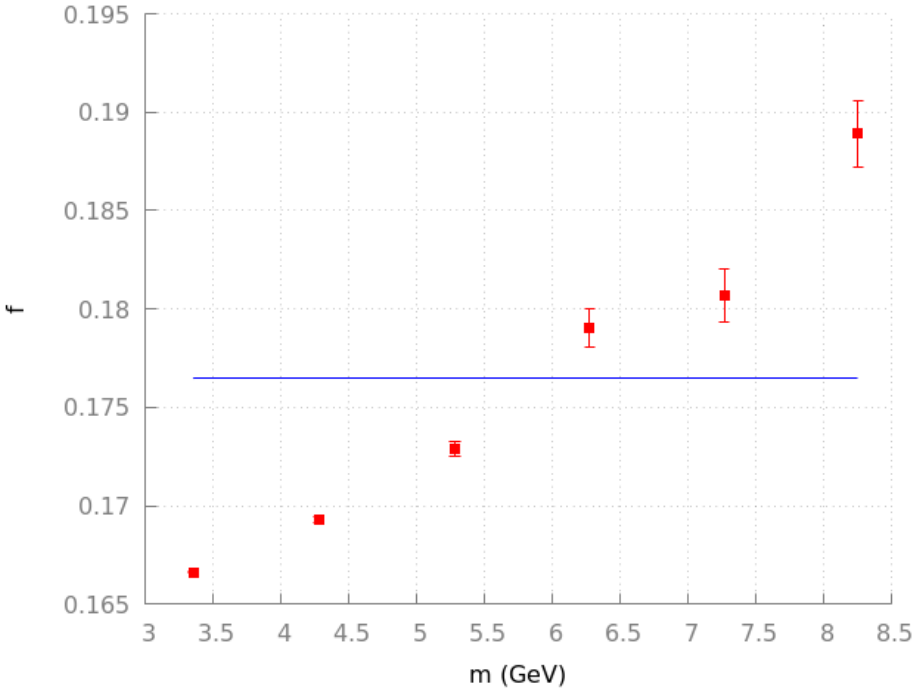

FIGURE 4.3: NH_3 dilution factor for Drell-Yan mass range. Also plotted is the static dilution factor of $\frac{3}{17} \approx 0.176$. Errors shown are entirely statistical.

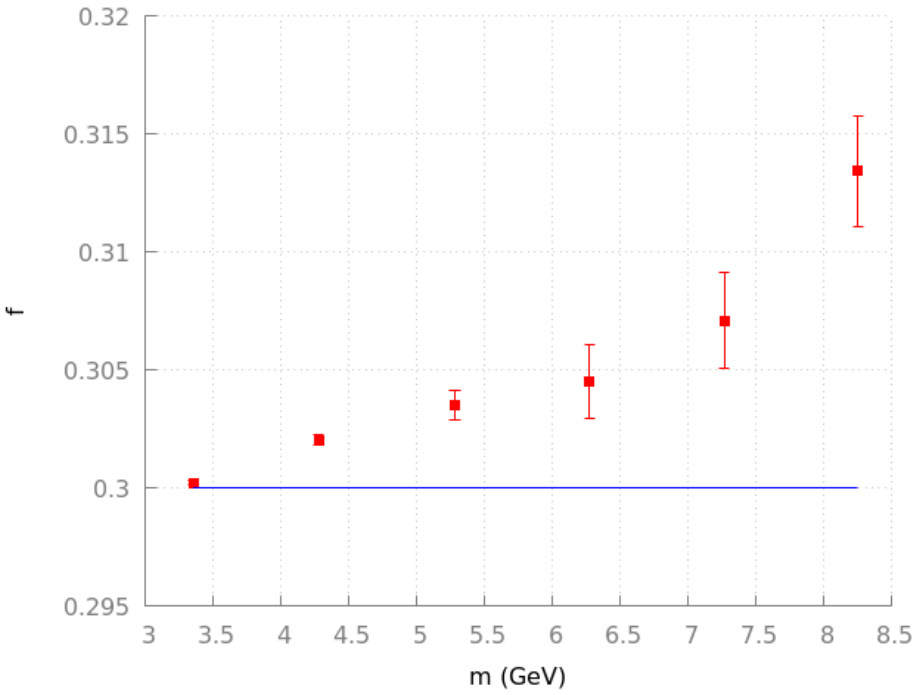

FIGURE 4.4: ND_3 dilution factor for Drell-Yan mass range. Also plotted is the static dilution factor of $\frac{6}{20} = 0.3$. Errors shown are entirely staistical.

M (GeV)	NH_3	ND_3
3-4	0.1666 ± 0.0001	0.3002 ± 0.0001
4-5	0.1693 ± 0.0001	0.3020 ± 0.0002
5-6	0.1729 ± 0.0004	0.3035 ± 0.0006
6-7	0.1790 ± 0.0010	0.3045 ± 0.0015
7-8	0.181 ± 0.001	0.307 ± 0.002
8-9	0.189 ± 0.002	0.313 ± 0.002

TABLE 4.2: Mass-dependent dilution factors for pure ammonia in the E1039 experiment. Errors are purely statistical.

Since the error in this analysis is only statistical, there is higher precision in the reported values. Similarly to the x_T dependent cross-section, the dilution factor changes more over the range for NH_3 than ND_3. Again, this is due to the difference in behavior of the differential cross-section of protons and heavy nuclei and the relative similarity of the behavior of the deuteron when compared to the same.

This suggests that since the dilution factor is dependent on the mass of the dilepton pair, the masses of the leptons included in the x_T analysis could affect the values reported. Since the dilution factor is lower for lower masses, higher lepton masses could increase the dilution factor, especially since x_T increases as mass increases.

4.2 Impacts on the Dilution Factor

In the experiment, there will be various factors that influence the exact value of the dilution factor. Some of these are due to decisions that will be made, while others will be random. In order to anticipate these factors, and thereby lower the systematic uncertainty of the experiment, a couple of factors that will affect the dilution factor of the target were explored.

4.2.1 Effect of mass-cuts on Dilution Factor

In Drell-Yan experiments, data to be analyzed is usually restricted by using mass-cuts, where dimuons that fall within certain mass ranges are not used, due to the J/Ψ and Υ processes which also results in dimuons. The J/Ψ cut is generally placed around 4 Gev, and the Υ cut generally excludes masses between 9 GeV and 11 Gev. There is a trade-off with the placement of the mass cut, since a lower cut will greatly increase the number of events (the integrated cross-section for $M_{ll} > 3$ GeV is around an order of magnitude larger than that for $M_{ll} > 4$ GeV), but will decrease the signal to noise ratio due to the J/Ψ process.

Because of the relationship between the dimuon invariant mass and x_T, the placement of the mass cut also affects the lowest possible value of x_T. This limit is given by

$$x_T \geq \frac{1}{2}(\sqrt{4\frac{M_{ll}^2}{s}} - 1) \tag{4.2}$$

Where $\sqrt{s}$ is the center-of-mass energy of the collision. For a lower mass cut of 4 GeV and a center-of-mass energy of 15.06 GeV (the energy for E1039), this gives a lower-limit of $x_T = 0.066$. The effect of the cuts will be seen over the entire x_T range, however, since it is also possible for low-mass dileptons to have higher x_T values.

In order to determine the effect of the mass-cuts on the dilution factor for each bin, MCFM simulations were run to determine the x-dependent cross-sections using a lower bound mass-cut at 3 GeV and a lower bound mass-cut at 4 GeV, as seen in figures. The Υ mass-cut was not included in this analysis, since the Drell-Yan cross-section in this range is 5 orders of magnitude lower than in the J/Ψ range.

These cross-sections were then used to calculate the dilution factors in each bin, and they were compared to each other by dividing the dilutions factor found from the 4 GeV mass-cut data by the dilution factors found from the 3 GeV mass-cut data. These ratios are shown in Figure 4.5 and in Table 4.3.

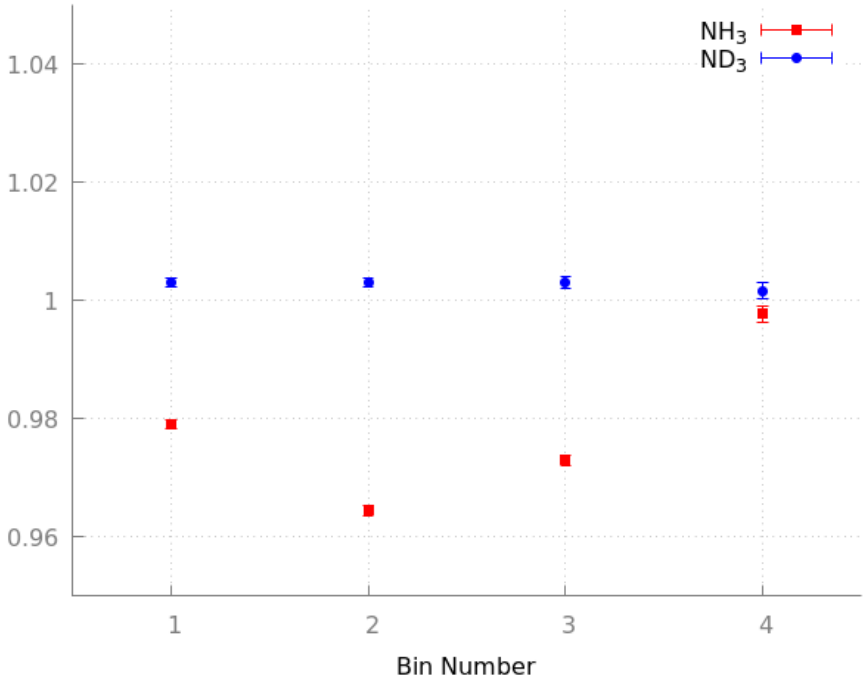

FIGURE 4.5: Ratio of dilution factors using 4 GeV and 3 GeV mass cuts in the E1039 x_T bins for NH_3 and ND_3. Errors shown are propagated reported from MCFM.

Bin	NH_3	ND_3
1	0.979	1.003
2	0.964	1.003
3	0.973	1.003
4	0.998	1.001

TABLE 4.3: Ratio of dilution factors using 4 GeV and 3 GeV mass cuts. All values have an associated error of ± 0.001.

It is clear from these simulations that the mass-cuts do indeed have an effect on the dilution factor for each of the bins. Interestingly, it seems to have opposite effects on NH_3 and ND_3.

The effect seems to be larger for NH_3 than for ND_3, which we would expect, as other parts of this analysis have suggested a lower degree of variability of the dilution factor of ND_3. For ND_3 this difference is small enough that it would not be noticed next to systematic uncertainties. For NH_3, however, the difference is

enough to merit a recalculation of these dilution factors once a mass-cut is chosen for the E1039 data.

4.2.2 Target Composition Dependence

Thus far, all of the dilution factors shown have been that of pure ammonia. In the actual experiment the other materials in the beam path will also influence the dilution factor. Although the experiment is designed to minimize the contributions of these materials, there will be some scattering from them that must be accounted for.

The largest influence and the greatest uncertainty will come from the ratio of helium and ammonia in the target cup. Due to the contraction of solid ammonia and the method used to fill the cup, there may be a relevant uncertainty in the ratio of the two materials.

Since this directly impacts the dilution factor, the dilution factor was calculated for a target containing different ratios of ammonia and helium. This was done by modifying the spreadsheet used to calculate the x_T-dependent dilution factor to include the unpolarizable helium in the denominator of the dilution factor. The ratio was defined as the percent of molecules that were ammonia, or

$$\%NH_3 = \frac{N(NH_3)}{N(NH_3) + N(He)} \tag{4.3}$$

This calculation was done using the same cross-section data as for the x-dependent dilution factor, and the bins were the same as those for E1039. The results are shown in Figure 4.6.

As expected, the ratio of ammonia to helium has a large impact on the dilution factor, increasing by 24% and 20% over the range for NH_3 and ND_3 respectively. This difference is due to deuterium having a larger cross-section than hydrogen, and thus ND_3 having a larger cross-section than NH_3.

By calculating the rate of change of these plots, it is possible to determine an estimated uncertainty introduced into the dilution factor value dependent on the uncertainty in the packing fraction. Since the relationship is not linear, the range was divided into five sections, and the uncertainty in the dilution factor based

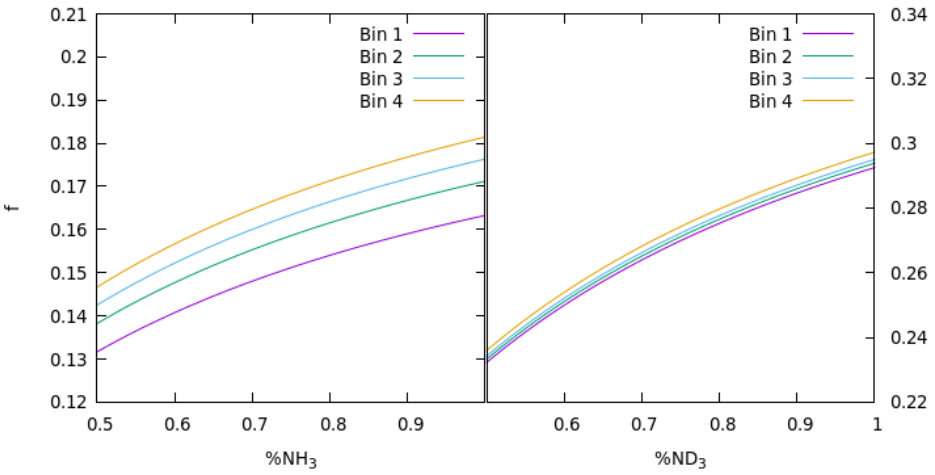

FIGURE 4.6: Dilution factor for mixtures of ammonia and helium for different ratios of ammonia.

on uncertainties in the packing fraction of 1%-5% was estimated for each section. These values can be seen in Tables 4.4 and 4.5.

$\%NH_3$/PF Error	1%	2%	3%	4%	5%
0.5-0.6	0.7%	1.4%	2.0%	2.7%	3.4%
0.6-0.7	0.5%	1.1%	1.6%	2.2%	2.8%
0.7-0.8	0.4%	0.8%	1.2%	1.7%	2.1%
0.8-0.9	0.3%	0.7%	1.0%	1.4%	1.7%
0.9-1.0	0.3%	0.5%	0.8%	1.1%	1.4%

TABLE 4.4: Error introduced to the dilution factor by uncertainties in the packing fraction for NH_3.

$\%ND_3$/PF Error	1%	2%	3%	4%	5%
0.5-0.6	0.6%	1.2%	1.8%	2.3%	2.9%
0.6-0.7	0.4%	0.9%	1.4%	1.9%	2.4%
0.7-0.8	0.3%	0.7%	1.1%	1.4%	1.8%
0.8-0.9	0.3%	0.6%	0.8%	1.1%	1.4%
0.9-1.0	0.2%	0.5%	0.5%	0.9%	1.2%

TABLE 4.5: Error introduced to the dilution factor by uncertainties in the packing fraction for ND_3.

These numbers are very encouraging for the overall systematic uncertainty of the experiment as a whole. Prior to this analysis the assumed uncertainty in the packing fraction of 2% contributed directly to the uncertainty. However, according to this analysis an uncertainty of 2% in the packing fraction would contribute less than 1% uncertainty to the analysis as a whole.

4.3 Target Composition Measurement

This analysis has exampined the dilution factor of an idealized target, either consisting entirely of ammonia or a precise mixture of ammonia and helium. The real target will contain other materials than these, and the amounts of each material and their contributions will not be perfectly known. There will be five materials in the target that can contribute to the detected events:

- Ammonia (NH_3 or ND_3)
- Helium
- Aluminum
- Kel-F (Polychlorotrifluoroethylene: F_3C_2Cl)
- Cupronickel (70% Cu, 30% Ni)

By determining the number of molecules of each of these in the target, as well as the average luminosity delivered to each material, it will be possible to accurately calculate the dilution factor for the physical target when used in conjuncture with their Drell-Yan cross-sections. This will allow us to reduce the total systematic uncertainty of the experiment by having a more accurately calculated dilution factor.

4.3.1 Packing Fraction

Due to radiation damage, the ammonia becomes less polarizeable as it is spends time in the beam, and must be replaced regularly. This refilling process adds uncertainty to the exact amount of ammonia and by extension the amount of helium in the target. The Kel-F, aluminum and cupronickel are the plastic of the target cup, the target windows, and the NMR coils, respectively. These do not have to be replaced during the experiment, so their amounts can be known more exactly.

Ammonia is stored in liquid nitrogen before it is used in the experiment, and put into the target cups at this temperature (77K). It will contract when submerged in liquid helium, and uncertainty in its density at 1K adds an uncertainty to the

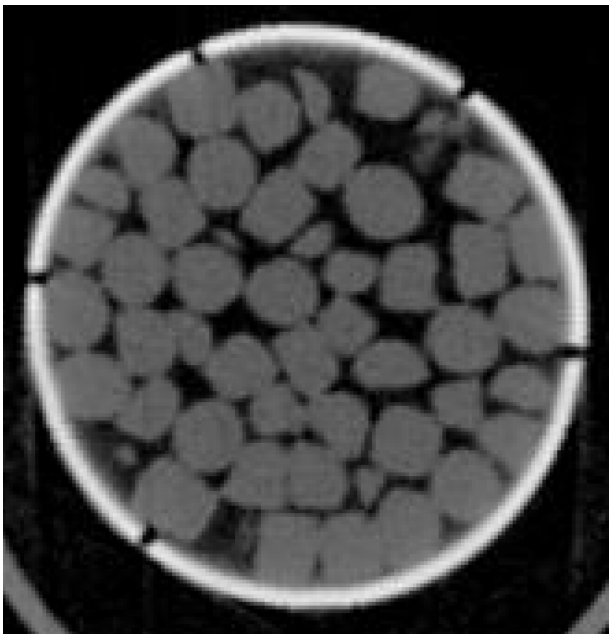

FIGURE 4.7: Cross-sectional image of the interior of a target cup using Bruker Trimodal PET/SPECT/CT Imager. Image is of polyethylene beads in a Kel-F target cup.

ratio of ammonia to helium. This uncertainty could be reduced in a couple of ways.

One possibility is to make a precise measurement of the density of solid ammonia. This would be done at liquid ammonia temperatures in order to narrow the prediction from lattice constants of the density at liquid helium temperatures. A plan has been made to use evaporation rate of liquid nitrogen to infer a volume measurement for a Archimedes' method measurement of the density of ammonia.

Another possibility is using micro CT scanning technology to image the target while submerged in liquid nitrogen. This will theoretically allow us to know the portion of the target filled by ammonia. The downside to this method is the potential cost of using the machine, and uncertainty in its ability to resolve the barrier between the cryogenic fluid and the solid ammonia. A recent test using polyethylene beads showed that the technology is able to resolve the inside of the cup with high precision, as seen in Figure 4.7

4.3.2 Luminosity Analysis

In order to predict the number of events contributed from each material, it is important to know the relative luminosity of the beam on each material. It may be assumed that, due to its location on the outer edge of the target, the Kel-F will not receive as high a luminosity as the aluminum, ammonia or helium, due to their location directly in the path of the beam.

To do this, once the composition of the target has been determined, a three-dimension model of the target should be constructed, and used in conjuncture with a model of the beam distribution to determine the average intensity delivered to each material.

By combining this average intensity value with the cross-section data for each of the materials, it will then be possible to make a properly weighted dilution factor calculation. A similar analysis to that found in section 4.4 of this thesis should then be done to determine the uncertainty arising from this analysis.

Chapter 5

Summary and Conclusions

By using Monte Carlo methods, it was possible to lower the uncertainty in the dilution factor, which contributes a significant amount of systematic error to the experiment as a whole. It was also possible to use that analysis to better understand how other systematic error sources contribute to the error as a whole. Namely, uncertainty in the packing fraction is now able to be tied directly to the uncertainty in the target's dilution factor.

It would be useful to compare MCFM data with cross-section data using the detector for E1039. By doing so, it would be possible to better tune the process to the specific kinematics of the experiment. This would lower the systematic uncertainties in the cross-sections generated by the program, which would in turn lower the systematic uncertainty of the calculated dilution factor.

Monte Carlo simulations can only go so far in reducing the systematic error since there are effects that do not have to do with the scattering, but instead involve uncertainties in physical quantities. These can be lowered by careful measurements or by improving equipment and procedures, but not as easily by analysis. MCFM then, is useful for calculating the contributions to the total dilution factor from each material, but is silent on the size of their contributions.

In order to reduce systematic uncertainty more, the work in an accurate packing fraction measurement should continue, as should the measurement of the density of solid ammonia. Not covered in this thesis are the contributions to the systematic error from the polarization and polarization measurements of the target, which also should be studied in order to lower their contributions.

Since the Sivers function asymmetry for sea quarks is thought to be very small, it is very important that sources of error be minimized for the experiment. Since a non-zero measured value suggests a non-zero orbital angular momentum, the value has importance to our understanding of the spin structure of the nucleon. Reducing uncertainty in the measured value would therefore give us more confidence in this understanding.

Bibliography

[1] Christian Wiese, Constantia Alexandrou, Martha Constantinou, Kyriakos Hadjiyiannakou, Christos Kallidonis, Giannis Koutsou, Karl Jansen, Haralambos Panagopoulos, Fernanda Steffens, and Alejandro Vaquero. Recent results for the proton spin decomposition from lattice qcd. *Proceedings of XXIV International Workshop on Deep-Inelastic Scattering and Related Subjects PoS(DIS2016)*, Nov 2016. doi: 10.22323/1.265.0240. URL http://dx.doi.org/10.22323/1.265.0240.

[2] L. A. Harland-Lang, A. D. Martin, P. Motylinski, and R. S. Thorne. Parton distributions in the lhc era: Mmht 2014 pdfs. *The European Physical Journal C*, 75(5), May 2015. ISSN 1434-6052. doi: 10.1140/epjc/s10052-015-3397-6. URL http://dx.doi.org/10.1140/epjc/s10052-015-3397-6.

[3] A. Baldit et al. Study of the isospin symmetry breaking in the light quark sea of the nucleon from the Drell-Yan process. *Phys. Lett.*, B332:244–250, 1994. doi: 10.1016/0370-2693(94)90884-2.

[4] A. et al Accardi. Electron-ion collider: The next qcd frontier. *The European Physical Journal A*, 52(9):268, Sep 2016. ISSN 1434-601X. doi: 10.1140/epja/i2016-16268-9. URL https://doi.org/10.1140/epja/i2016-16268-9.

[5] CMS Collaboration. Measurement of the differential drell-yan cross section in proton-proton collisions at $\sqrt{s} = 13$ tev, 2018.

[6] Stanley J. Brodsky, Dae Sung Hwang, and Ivan Schmidt. Final-state interactions and single-spin asymmetries in semi-inclusive deep inelastic scattering. *Physics Letters B*, 530(1-4):99107, Mar 2002. ISSN 0370-2693. doi: 10.1016/s0370-2693(02)01320-5. URL http://dx.doi.org/10.1016/S0370-2693(02)01320-5.

[7] Xiaoyu Wang and Zhun Lu. Sivers asymmetry in the pion induced Drell-Yan process at COMPASS within transverse momentum dependent factorization. *Phys. Rev.*, D97(5):054005, 2018. doi: 10.1103/PhysRevD.97.054005.

[8] K. et al. Allada. Single spin asymmetries of inclusive hadrons produced in electron scattering from a transversely polarized ^{3}he target. *Phys. Rev. C*, 89: 042201, Apr 2014. doi: 10.1103/PhysRevC.89.042201. URL https://link.aps.org/doi/10.1103/PhysRevC.89.042201.

[9] Murray Gell-Mann. A Schematic Model of Baryons and Mesons. *Physics Letters*, 8:214–215, 1964.

[10] George Zweig. An SU(3) Model for Strong Interaction Symmetry and its Breaking. *CERN Report*, No8182:TH.401, 1964.

[11] Richard Feynman. Very High-Energy Collisions of Hadrons. *Phys. Rev. Lett.*, 23(24):1415–1417, Dec 1969.

[12] B. Povh; C. Scholz; K. Rith; F. Zetsche. *Particles and Nuclei*. Springer, 2008. ISBN 978-3-540-79367-0.

[13] J; EMC Collaboration Ashman. A measurement of the spin asymmetry and determination of the structure function g1 in deep inelastic muon-proton scattering. *Physics Letters B*, 206(2):364, Dec 1987.

[14] Huey-Wen Lin, Emanuele R. Nocera, Fred Olness, Kostas Orginos, Juan Rojo, Alberto Accardi, Constantia Alexandrou, Alessandro Bacchetta, Giuseppe Bozzi, Jiunn-Wei Chen, and et al. Parton distributions and lattice qcd calculations: A community white paper. *Progress in Particle and Nuclear Physics*, 100:107160, May 2018. ISSN 0146-6410. doi: 10.1016/j.ppnp.2018.01.007. URL http://dx.doi.org/10.1016/j.ppnp.2018.01.007.

[15] Z. Kunszt. From scattering amplitudes to cross sections in qcd, 1996.

[16] Sidney D. Drell and Tung-Mow Yan. Massive lepton-pair production in hadron-hadron collisions at high energies. *Phys. Rev. Lett.*, 25:316–320, Aug 1970. doi: 10.1103/PhysRevLett.25.316. URL https://link.aps.org/doi/10.1103/PhysRevLett.25.316.

[17] M. Anselmino, M. Boglione, U. D'Alesio, S. Melis, F. Murgia, and A. Prokudin. Sivers effect in drell-yan processes. *Phys. Rev. D*, 79:054010,

Mar 2009. doi: 10.1103/PhysRevD.79.054010. URL https://link.aps.org/doi/10.1103/PhysRevD.79.054010.

[18] I R Kenyon. The drell-yan process. *Reports on Progress in Physics*, 45 (11):1261–1315, nov 1982. doi: 10.1088/0034-4885/45/11/002. URL https://doi.org/10.1088%2F0034-4885%2F45%2F11%2F002.

[19] Jai More, Asmita Mukherjee, and Sreeraj Nair. Wigner distributions of quarks for different polarizations. *Few-Body Systems*, 58(2), Jan 2017. ISSN 1432-5411. doi: 10.1007/s00601-016-1207-9. URL http://dx.doi.org/10.1007/s00601-016-1207-9.

[20] Davison E. Soper. Parton distribution functions. *Nuclear Physics B - Proceedings Supplements*, 53(1-3):6980, Feb 1997. ISSN 0920-5632. doi: 10.1016/s0920-5632(96)00600-7. URL http://dx.doi.org/10.1016/S0920-5632(96)00600-7.

[21] E. D. Bloom, D. H. Coward, H. DeStaebler, J. Drees, G. Miller, L. W. Mo, R. E. Taylor, M. Breidenbach, J. I. Friedman, G. C. Hartmann, and H. W. Kendall. High-energy inelastic $e - p$ scattering at 6 and 10 degrees. *Phys. Rev. Lett.*, 23:930–934, Oct 1969. doi: 10.1103/PhysRevLett.23.930. URL https://link.aps.org/doi/10.1103/PhysRevLett.23.930.

[22] Harald Fritzsch and Murray Gell-Mann. *50 years of quarks. Fifty years of quarks*. World Scientific, Hackensack, NJ, Mar 2015. doi: 9814618098. URL http://cds.cern.ch/record/1954513.

[23] S. Kumano. Flavor asymmetry of antiquark distributions in the nucleon. *Physics Reports*, 303(4):183257, Sep 1998. ISSN 0370-1573. doi: 10.1016/s0370-1573(98)00016-7. URL http://dx.doi.org/10.1016/S0370-1573(98)00016-7.

[24] Fermilab E866/NuSea Collaboration. Measurement of the light antiquark flavor asymmetry in the nucleon sea. *Phys. Rev. Lett.*, 80:3715–3718, Apr 1998. doi: 10.1103/PhysRevLett.80.3715. URL https://link.aps.org/doi/10.1103/PhysRevLett.80.3715.

[25] J. J. Aubert et al. The ratio of the nucleon structure functions $F2_n$ for iron and deuterium. *Phys. Lett.*, 123B:275–278, 1983. doi: 10.1016/0370-2693(83)90437-9.

[26] J. Arrington, A. Daniel, D. B. Day, N. Fomin, D. Gaskell, and P. Solvignon. Detailed study of the nuclear dependence of the emc effect and short-range correlations. *Physical Review C*, 86(6), Dec 2012. ISSN 1089-490X. doi: 10.1103/physrevc.86.065204. URL http://dx.doi.org/10.1103/PhysRevC.86.065204.

[27] P R Norton. The EMC effect. *Reports on Progress in Physics*, 66(8):1253–1297, jul 2003. doi: 10.1088/0034-4885/66/8/201. URL https://doi.org/10.1088%2F0034-4885%2F66%2F8%2F201.

[28] Evgenii Mitrofanov. Emc effect in the drell-yan process at compass. *EPJ Web of Conferences*, 177:04006, 01 2018. doi: 10.1051/epjconf/201817704006.

[29] J. Arrington, A. Daniel, D. B. Day, N. Fomin, D. Gaskell, and P. Solvignon. Detailed study of the nuclear dependence of the emc effect and short-range correlations. *Physical Review C*, 86(6), Dec 2012. ISSN 1089-490X. doi: 10.1103/physrevc.86.065204. URL http://dx.doi.org/10.1103/PhysRevC.86.065204.

[30] I. Schienbein, J. Y. Yu, K. Kovak, C. Keppel, J. G. Morfn, F. I. Olness, and J. F. Owens. Parton distribution function nuclear corrections for charged lepton and neutrino deep inelastic scattering processes. *Physical Review D*, 80(9), Nov 2009. ISSN 1550-2368. doi: 10.1103/physrevd.80.094004. URL http://dx.doi.org/10.1103/PhysRevD.80.094004.

[31] K. Kovarik. Update and comparison of nuclear parton distribution functions and neutrino dis, 2012.

[32] Dennis Sivers. Single-spin production asymmetries from the hard scattering of pointlike constituents. *Phys. Rev. D*, 41:83–90, Jan 1990. doi: 10.1103/PhysRevD.41.83. URL https://link.aps.org/doi/10.1103/PhysRevD.41.83.

[33] John M. Campbell, R. Keith Ellis, and Walter T. Giele. A multi-threaded version of mcfm, 2015.

[34] S. Catani and M.H. Seymour. A general algorithm for calculating jet cross sections in nlo qcd. *Nuclear Physics B*, 485(1-2):291419, Feb 1997. ISSN 0550-3213. doi: 10.1016/s0550-3213(96)00589-5. URL http://dx.doi.org/10.1016/S0550-3213(96)00589-5.

[35] G Peter Lepage. A new algorithm for adaptive multidimensional integration. *Journal of Computational Physics*, 27(2):192 – 203, 1978. ISSN 0021-9991. doi: https://doi.org/10.1016/0021-9991(78)90004-9. URL http://www.sciencedirect.com/science/article/pii/0021999178900049.

[36] Pavel M. et al. Nadolsky. Implications of CTEQ global analysis for collider observables. *Phys. Rev.*, D78:013004, 2008. doi: 10.1103/PhysRevD.78.013004.

[37] C.A. Aidala et al. The seaquest spectrometer at fermilab. *Nuclear Instruments and Methods in Physics Research Section A: Accelerators, Spectrometers, Detectors and Associated Equipment*, 930:49 – 63, 2019. ISSN 0168-9002. doi: https://doi.org/10.1016/j.nima.2019.03.039. URL http://www.sciencedirect.com/science/article/pii/S016890021930347X.

[38] B. Schmookler et al. Modified structure of protons and neutrons in correlated pairs. *Nature*, 566(7744):354–358, 2019. doi: 10.1038/s41586-019-0925-9.

MCFM Dilution Factor Instructions

This analysis was done with MCFM version 8.3, but during the work an updated version was released. Using the most recent version is preferred, as newer versions include more recent PDFs, which increase the accuracy of the predictions. All nessesary files can be found at mcfm.fnal.gov.

After downloading the zip file, extract the files into the desired directory and follow the installation instructions. It is possible that you may need to update compilers, and there may be other errors that need to be corrected. The make file and installation provide feedback if it is unable to compile on your machine.

Once installed, you need to edit the file src/User/userplotter.f to include the Fermi-x and Bjorken-x cross sections of the process that you are analyzing. Chosen cuts for this process should also be done in this section. For instance, E1039 only considers events with $x_f > 0$, so an if statement checking the value of x_f was added, making negative x_f value events not contribute to calculated cross-sections.

Next, the input file (input.DAT), located in the Bin directory needs to be edited. There are many parameters in this that can be edited, such as the order of the perturbation theory used in the calculation (next-to leading order is default), the process to be analyzed (a table is located in Doc/mcfm.pdf), the QCD scale, the masses of various particles used in the simulation, and cuts that can be used to isolate a certain range of the dynamics of the scattering.

Also in this file are the ability to select the particles being scattered (proton signified by +1, antiproton by -1, and nuclear particles by the number $1000Z + A$, where Z is the atomic number and A is the atomic mass of the nucleus.)

Additionally, you can set the number of events per iteration of the simulation, as well as the number of iterations that the program will average over.

A good strategy is to create a directory within the Bin directory that contains multiple input files that can be used for various target particles. The program needs to be directed to these input files, by using the command "./mcfm_omp Path/To/file.DAT" to run the program. If the program is run without a specified input file, it will default to a file called "input.DAT" in the current directory. If there is no such file, the program will not run.

Once the input files are correct, as well as the output histograms tuned to the desired range and precision, you can run the program. It is suggested to use different runstrings (specified in the input file) to prevent overwriting prior runs. If you are using the program for a process other than Drell-Yan, you should find published cross-section data from a few experiments to compare MCFM to real data. By doing so, you can establish systematic uncertainty for the process you are using.

To do this, you should compare the experimental data to the simulated cross-sections. The deviation of the MCFM calculated values from the experimental values can be used as an estimate of the systematic error. If possible, as much data as possible should be compared, and their deviations averaged to estimate the systematic error.

Once you have the differential cross-sections for all of the necessary nuclei, you can calculate the dynamic-dependent dilution factor. It is easiest to use a spreadsheet to do this, such as the one found at twist.phys.virginia.edu/(enter address). If you are calculating for specific bins, it is important to weight the average dilution factor over this range by the cross-section of the target. Also important is the correct propagation of error.